A material point/finite volume method for coupled shallow water flows and large dynamic deformations in seabeds

Zheng, Xiangcou; Seaid, Mohammed; Pisanò, Federico; Hicks, Michael A.; Vardon, Philip J.; Huvaj, Nejan; Osman, Ashraf S.

DOI
10.1016/j.compgeo.2023.105673

Publication date
2023

Document Version
Final published version

Published in
Computers and Geotechnics

Citation (APA)
Zheng, X., Seaid, M., Pisanò, F., Hicks, M. A., Vardon, P. J., Huvaj, N., & Osman, A. S. (2023). A material point/finite volume method for coupled shallow water flows and large dynamic deformations in seabeds. *Computers and Geotechnics*, *162*, Article 105673. https://doi.org/10.1016/j.compgeo.2023.105673

Computers and Geotechnics 162 (2023) 105673

Contents lists available at ScienceDirect

Computers and Geotechnics

journal homepage: www.elsevier.com/locate/compgeo

Research Paper

A material point/finite volume method for coupled shallow water flows and large dynamic deformations in seabeds

Xiangcou Zheng [a,*], Mohammed Seaid [a], Federico Pisanò [b], Michael A. Hicks [b], Philip J. Vardon [b], Nejan Huvaj [c], Ashraf S. Osman [a]

[a] Department of Engineering, University of Durham, South Road, Durham, DH1 3LE, United Kingdom
[b] Geo-Engineering Section, Faculty of Civil Engineering and Geosciences, Delft University of Technology, Delft, The Netherlands
[c] Department of Civil Engineering, Middle East Technical University, Ankara 06800, Turkiye

ARTICLE INFO

Keywords:
Finite volume method
Hybrid methods
Large deformation analysis
Material point method
Shallow water flows

ABSTRACT

A hybrid material point/finite volume method for the numerical simulation of shallow water waves caused by large dynamic deformations in the bathymetry is presented. The proposed model consists of coupling the nonlinear shallow water equations for the water flow and a dynamic elastoplastic system for the seabed deformation. As a constitutive law, we consider a linear elastic-non-associative plastic model with the Drucker-Prager yield criterion allowing for large deformations under undrained cases. The transfer conditions between these models are achieved by using forces sampled from the hydraulic pressure and the friction terms along the interface between the seabed soil and shallow water. A detailed description regarding the coupled algorithm for the hybrid material point/finite volume method is presented. Several numerical examples are investigated to demonstrate the performance of the finite volume method for simulations of shallow water flow and the material point method for capturing the large deformation process of the solid phase. We also present numerical simulations of an undrained clay column collapse that induced shallow water waves and a dam-break problem to demonstrate the excellent performance of the proposed hybrid material point/finite volume method.

1. Introduction

The numerical simulation of shallow water waves induced by large dynamic deformations in the bathymetry is extremely relevant to a number of geotechnical problems, such as submarine and/or subaerial landslides. Water waves generated by the deformation of the seabed are of general interest to coastal and ocean engineering. The study of bed deformations is of great complexity since it is a class of natural phenomena that occur under certain conditions such as earthquakes, water mass movements, storms and heavy rainfalls; see for example Hargarten and Robl (2019), Kirstetter et al. (2016), and Ramadan et al. (2011). In such events, bed deformations are capable of generating several types of long waves due to the energy transfer to the water volume. Free-surface waves generated by bed deformations include very powerful and destructive tsunami waves, which propagate and produce catastrophic waves causing significant coastal run-up (Fuhrman and Madsen, 2009; Zhang et al., 2019). In recent years, a considerable research effort has been developed regarding the mathematical modelling and numerical simulation of the interaction between bed deformation and water waves, as well as the mechanisms of surface gravity wave generation and propagation. In general, the modelling of wave run-up by static deformation is based on two components, these being the description of the bed deformation and the governing equations of the water motion. Numerous investigations for the waves induced by the deformations in seabeds have been carried out since the 1970s, see for example Zhang et al. (2015), Chen et al. (2010), Koukouselis et al. (2019), and Cremonesi et al. (2011). Numerical simulations have also been widely carried out to examine the problem in recent years. Fuhrman and Madsen (2009) studied a buried pipeline in a region that is surrounded by two impermeable walls. Magda (1997) considered a similar case with a wider range of degree of saturation, whereas soil-pipeline contact effects and inertial forces in a new model were investigated by Luan et al. (2008). In experimental investigations, the research contributions can be distinguished into two parts: (i) field measurements and (ii) laboratory experiments. In the field measurement studies, data for water pressure at the seabed surface, and for pore water pressure and vertical and horizontal total stresses in the seabed, have been collected, analyzed and compared with their theoretical counterparts in Okusa and Uchilda (1980), Okusa (1985), and Zen and Yamazaki (1991)

* Corresponding author.
E-mail addresses: xiangcou.zheng@durham.ac.uk, xczheng@csu.edu.cn (X. Zheng), m.seaid@durham.ac.uk (M. Seaid), F.Pisano@tudelft.nl (F. Pisanò), M.A.Hicks@tudelft.nl (M.A. Hicks), p.j.vardon@tudelft.nl (P.J. Vardon), nejan@metu.edu.tr (N. Huvaj), ashraf.osman@durham.ac.uk (A.S. Osman).

https://doi.org/10.1016/j.compgeo.2023.105673
Received 17 February 2023; Received in revised form 2 June 2023; Accepted 15 July 2023
Available online 1 August 2023

among others. In laboratory experimental studies (Tsui and Helfrich, 1983), the pore pressures in the seabed induced by progressive waves in wave flumes have been studied and compared with the results derived from linear wave theory. On the other hand, several numerical algorithms have been proposed to accommodate complex geometry and physical conditions. For example, Pudykiewicz and Staniforth (1984) developed a simplified finite element model for isotropic and saturated permeable seabeds. In order to improve the computational efficiency, a radial point interpolation meshless method was implemented in Wang et al. (2004).

In many cases, traditional mesh-based methods such as the Finite Element Method (FEM) show significant limitations when simulating these large deformation problems. For example, the intrinsic defects of the FEM frequently lead to aborted numerical simulations or misleading results due to excessive mesh distortions for problems involving large deformations. To remedy these mesh-distortion issues, several specific remeshing techniques have been proposed (Nazem et al., 2008; Wang et al., 2015). As an alternative, some meshfree/meshless methods, such as the Smoothed Particle Hydrodynamics (SPH) method (Gingold and Monaghan, 1977; Monaghan, 1994; Pastor et al., 2014, 2018), the Material Point Method (MPM) (Sulsky et al., 1994, 1995), the element-free Galerkin method (Belytschko et al., 1995), the Particle Finite Element Method (PFEM) (Oñate et al., 2004; Monforte et al., 2017; Della Vecchia et al., 2019; Yuan et al., 2020, 2021b) and other mesh-free methods (Li et al., 2010, 2014; Navas et al., 2016, 2018), have also been proposed to solve large deformation geotechnical problems, with each one featuring a specific mixture of advantages and drawbacks. The well-developed Material Point Method (MPM) was derived from the Particle-in-cell (PIC) method that was originally developed for solving complex fluid mechanics problems. It is known that MPM combines the advantages of both Eulerian and Lagrangian approaches, and it effectively avoids the treatment of convection terms in the Eulerian formulation and excessive mesh distortion in the Lagrangian formulation. For this reason, it has been gaining recognition as a robust approach for the simulation of large deformation geotechnical problems, such as landslides (Andersen, 2009; Andersen and Andersen, 2010; Soga et al., 2015; Wang et al., 2018; Yerro et al., 2019), the bearing capacity of footings (Kiriyama and Higo, 2020; Bisht et al., 2021; Wang et al., 2021), anchor pull-out (Coetzee et al., 2005; Ceccato et al., 2020; Liang et al., 2021), and cone penetration (Beuth, 2012; Ceccato et al., 2016; Martinelli and Galavi, 2021). It is also the approach that was preferred in this study.

In the context of MPM, both single-layer and two-layer approaches have been explored, *i.e.*, the use of one or two sets of material points to describe the interaction between solid and fluid phases. When using a single-layer of material points, the position of a material point is updated following the movement of the solid phase. Even though this approach only guarantees mass conservation of the solid phase, the lower computational costs that are associated with the single-layer approach have motivated its frequent use in previous coupled MPM research (Zhang et al., 2009; Zabala and Alonso, 2011; Jassim et al., 2013; Zheng et al., 2013; Ceccato et al., 2016; Lei et al., 2021; Zhao and Choo, 2020; Zheng et al., 2021, 2022; Zheng, 2022). Conversely, two sets of material points, *i.e.*, a solid layer and a water layer, have also been used (Zhang et al., 2007; Abe et al., 2013; Bandara and Soga, 2015; Liu et al., 2017; Tran and Sołowski, 2019; Kularathna et al., 2021; Zhao et al., 2022; Du et al., 2021), which can easily guarantee the mass conservation of both phases and capture the interaction between them. In the two-layer approach, the two sets of material points are respectively used for tracking the motion of the solid and water phases (Soga et al., 2015), which may be more suitable for simulating the type of problem considered in this study. However, despite its proven robustness, it is known that the presence of two layers of material points leads to a significant increase in computational costs. Moreover, when involving a nearly or fully incompressible free water phase, MPM suffers from spurious pore pressure oscillations and free-surface instabilities (Zheng, 2022), and special treatments are generally required for detecting the free water surface. Thus, more robust and efficient methods are required to simulate the coupled shallow water flows and large deformations in seabeds. With this in mind, it is known that the Finite Volume Method (FVM) has a key advantage in simulating the dynamic flow of shallow water owing to its natural conservation of mass, momentum, and energy. Therefore, the FVM can be viewed as an ideal replacement for the MPM for simulating the dynamic motion of the shallow water, and it has been coupled with MPM in the study of Baumgarten et al. (2021). In the present study, we propose a hybrid material point/finite volume method for the modelling and numerical simulation of shallow water waves caused by undrained large dynamic deformations in the bed topography. This is achieved by incorporating a depth-averaged robust FVM solver and a novel interface coupling algorithm between the MPM and FVM techniques. For the proposed method, MPM is adopted to solve the equations that govern the undrained large deformation of the seabed soils by a Lagrangian description, whereas the robust FVM is applied to the governing equations of the shallow water in an Eulerian context. The coupled scheme between the MPM and FVM models is achieved using forces sampled from the hydraulic pressure and the friction terms along the interface between the seabed soil and shallow water. A detailed description regarding the coupled algorithm for the hybrid material point/finite volume method is presented. Several numerical examples are presented to demonstrate the performance of the proposed hybrid MPM/FVM and its capability in simulating shallow water waves caused by large dynamic deformations of the seabed.

The paper is organized as follows. A description of the coupled model for coupled shallow water flows and large dynamic deformations in seabeds is presented in Section 2. This section covers the governing equations for elastoplastic deformations in seabeds and shallow water flows, along with the coupling conditions between the two models. Section 3 is devoted to the formulation of the computational techniques used for the numerical solution procedure. We consider a two-dimensional MPM for the large dynamic deformations in seabeds, whereas a well-balanced finite volume method is implemented for the shallow water flows. In Section 4, we present numerical results for several examples of coupled shallow water flows and large dynamic deformations in seabeds. Concluding remarks are drawn in Section 5.

2. Modelling free-surface waves caused by soil deformations

In continuum mechanics, the two basic equations that govern the dynamic motion of the soil, namely the mass and momentum conservation equations, are written as follows:

$$\begin{aligned} &\frac{\mathrm{d}\rho}{\mathrm{d}t} + \rho\nabla\cdot\boldsymbol{v} = 0, \\ &\rho\frac{\mathrm{d}\boldsymbol{v}}{\mathrm{d}t} - \nabla\cdot\boldsymbol{\sigma} = \rho\boldsymbol{b}, \end{aligned} \tag{1}$$

where ρ is the mass density of the soil, $\boldsymbol{v}$ is the soil particle velocity, $\boldsymbol{\sigma}$ is the stress tensor, $\boldsymbol{b}$ is the external body force, ∇ is the gradient operator, and $(\cdot)$ indicates the inner product. It should be stressed that various constitutive models can be adopted for computing the stress tensor $\boldsymbol{\sigma}$ in Eqs. (1), without major conceptual modifications. In this study, the non-associative Drucker–Prager elastoplastic model, which has previously been chosen in the SPH simulation of large deformation geotechnical problems (Bui et al., 2008, 2014; Feng et al., 2021; Nguyen et al., 2017), is implemented in the proposed hybrid material point/finite volume method. Following this elastoplastic constitutive model, the stress–strain relationship can be expressed by

$$\dot{\boldsymbol{\sigma}} = \boldsymbol{D}^e : (\dot{\boldsymbol{\varepsilon}} - \dot{\boldsymbol{\varepsilon}}^p), \tag{2}$$

where $\dot{\boldsymbol{\sigma}}$ is the stress rate tensor, $\boldsymbol{D}^e$ is the elastic tangent stiffness tensor, and $\dot{\boldsymbol{\varepsilon}}$ is the total strain rate tensor which can be divided into two parts, namely, the elastic $\dot{\boldsymbol{\varepsilon}}^e$ and plastic $\dot{\boldsymbol{\varepsilon}}^p$ strain rates. Note that in

the considered Drucker–Prager elastoplastic model, the yield function f and plastic potential function g are defined by

$$f = \alpha_\phi I_1 + \sqrt{J_2} - k_c, \qquad g = \alpha_\psi I_1 + \sqrt{J_2}, \tag{3}$$

where I_1 is the first invariant of the stress tensor, J_2 is the second deviatoric stress invariant, α_ϕ and k_c are Drucker–Prager model parameters, and α_ψ is a dilatancy factor. Thus, the stress–strain relation can be written as

$$\dot{\sigma}_{ij} = 2G\dot{e}_{ij} + K\dot{\varepsilon}_{kk}\delta_{ij} - \dot{\lambda}\left(3K\alpha_\phi\delta_{ij} + \frac{G}{\sqrt{J_2}}s_{ij}\right), \tag{4}$$

where $\dot{\sigma}_{ij}$ is the stress rate tensor, $\dot{e}_{ij}$ is the deviatoric strain rate tensor, $\dot{\varepsilon}_{kk}$ is the trace of the strain rate tensor, δ_{ij} is the Kronecker delta, $\dot{\lambda}$ is the rate of change of plastic multiplier, s_{ij} is the deviatoric stress tensor, and G and K are the elastic shear and bulk moduli, respectively.

It should be noted that, for considering large deformation problems, the Jaumann rate, which gives an objective measure of the stress rate with respect to rigid-body rotation, is employed in the current study. Thus, the final form of the stress–strain relationship for the non-associative Drucker–Prager elastoplastic model is written as

$$\dot{\sigma}_{ij} = \sigma_{ik}\dot{\omega}_{jk} + \sigma_{kj}\dot{\omega}_{ik} + 2G\dot{e}_{ij} + K\dot{\varepsilon}_{kk}\delta_{ij} - \dot{\lambda}\left(3K\alpha_\phi\delta_{ij} + \frac{G}{\sqrt{J_2}}s_{ij}\right), \tag{5}$$

where $\dot{\varepsilon}_{ij}$ and $\dot{\omega}_{ij}$, respectively, define the strain rate and spin rate tensors given by

$$\dot{\varepsilon}_{ij} = \frac{1}{2}\left(\frac{\partial v_i}{\partial x_j} + \frac{\partial v_j}{\partial x_i}\right), \qquad \dot{\omega}_{ij} = \frac{1}{2}\left(\frac{\partial v_i}{\partial x_j} - \frac{\partial v_j}{\partial x_i}\right). \tag{6}$$

As a consequence of the large deformation of the soil, perturbations with different structures are expected to be generated on the water free-surface. In the present study, we consider a one-dimensional nonlinear shallow water system for modelling these free-surface flows. In general, the governing equations for shallow water flows are formulated in terms of the surface elevation η and the discharge q as (Pudjaprasetya and Ribal, 2009)

$$\begin{aligned} \frac{\partial \eta}{\partial t} + \frac{\partial q}{\partial x} &= 0, \\ \frac{\partial q}{\partial t} + \frac{\partial}{\partial x}\left(\frac{q^2}{\eta - B} + \frac{g}{2}\left(\eta^2 - 2\eta B\right)\right) &= -g\eta\frac{\partial B}{\partial x} - \tau_f, \end{aligned} \tag{7}$$

where $B(t,x)$ is the deformed bed, and $h(t,x)$ is the water depth with $\eta = h + B$. In (7), the discharge $q = hv$, where $v(t,x)$ is the water velocity and τ_f is the bed friction force defined by

$$\tau_f = gM_b^2\frac{v|v|}{h^{\frac{1}{3}}}, \tag{8}$$

where g is the gravitational acceleration and M_b is the Manning coefficient, see Fig. 1 for an illustration. Indeed, under the influence of gravity, many free-surface water flows can be accurately modelled by the shallow water equations with the assumption that the vertical scale is much smaller than any typical horizontal scale in the flow domain. These models are derived by depth-averaging the three-dimensional incompressible Navier–Stokes equations using appropriate free-surface and bed boundary conditions, along with the assumption that the pressure is purely hydrostatic. The shallow water Eqs. (7) have been successfully applied to many engineering problems and their fields of application include a wide spectrum of phenomena other than water waves. For example, the shallow water equations have been used for applications in hydraulics and environmental engineering, such as tidal flows in estuaries or coastal regions, rivers, reservoirs and open channel flows among others. Note that the first and second equations in the shallow water system Eqs. (7) represent, respectively, the continuity and momentum equations, and that they can be reformulated using the conservative variables h and hv as

$$\begin{aligned} \frac{\partial h}{\partial t} + \frac{\partial (hv)}{\partial x} &= 0, \\ \frac{\partial (hv)}{\partial t} + \frac{\partial}{\partial x}\left(hv^2 + \frac{1}{2}gh^2\right) &= -gh\frac{\partial B}{\partial x} - gM_b^2\frac{v|v|}{h^{\frac{1}{3}}}. \end{aligned} \tag{9}$$

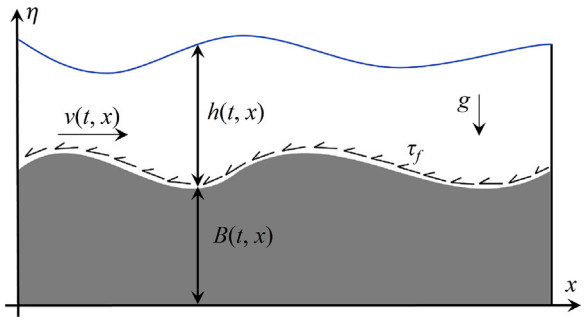

Fig. 1. Shallow water domain and notations.

For the numerical implementation, a splitting approach is used for the coupled models, for which large deformations in the bed and free-surface perturbations in the water are computed separately using the two-dimensional governing Eqs. (1) and the one-dimensional nonlinear shallow water Eqs. (9). The coupling between the two models is accounted for at the interface between the bed and the water by updating the bed topography $B(t,x)$ at each deformation stage. Notice that, for simplicity in the formulation, no sediment transport is considered in the current study. It should also be noted that the main limitations of the considered shallow water system Eqs. (9) are related to its failure to capture the vertical velocity in the water flow and it also cannot be used to model breaking waves in free-surface flows. For these types of applications, the full three-dimensional Navier–Stokes equations or multilayer shallow water models are required.

In our analysis, the responses of the water free-surface to large deformations in the seabed generated by Eqs. (1) are assessed using the shallow water system Eqs. (9), subject to the movable topography B which depends on space and time. On the other hand, the effects of water on the seabed are included on the interface using the vertical and horizontal forces respectively generated by the hydrostatic pressure and the friction term:

$$p = -\rho_w g\left(h - \eta_0\right), \qquad \tau_f = -gM_b^2\frac{v|v|}{h^{\frac{1}{3}}}, \tag{10}$$

where ρ_w is the water density, and $\eta_0 = h_0 + B$ with h_0 being the initial water depth. Note that responses of the water free-surface to deformations in the bed topography depend on the properties of the seabed soil, the magnitude of the applied force, and the initial water depth among others. It should also be noted that, in many applications in geotechnics, the impact of free-surface flows on the seabed is assumed to be negligible compared to the impact of bed deformations on the water free-surface, see for example Pudykiewicz and Staniforth (1984).

3. Hybrid material point/finite volume method

In the current work, to solve the coupled model for shallow water waves and large dynamic deformations in the seabed, MPM is adopted to capture the undrained elasto-plastic deformation process of the seabed and FVM is implemented for solving the shallow water system. In this preliminary study, a single seabed soil with a total stress analysis is considered. For the purpose of completeness, the fundamentals of MPM, and the numerical formulation and implementation of both MPM and FVM, are briefly summarized in this section. Notice that the emphasis is on a detailed description of the coupled solution algorithm between MPM and FVM for solving the coupled system Eqs. (1) and Eqs. (9).

3.1. Material point method for bed deformations

As a variant of conventional FEM, MPM inherits advantages of both Eulerian and Lagrangian approaches by adopting two different discretizations: a fixed Eulerian background grid and moving Lagrangian

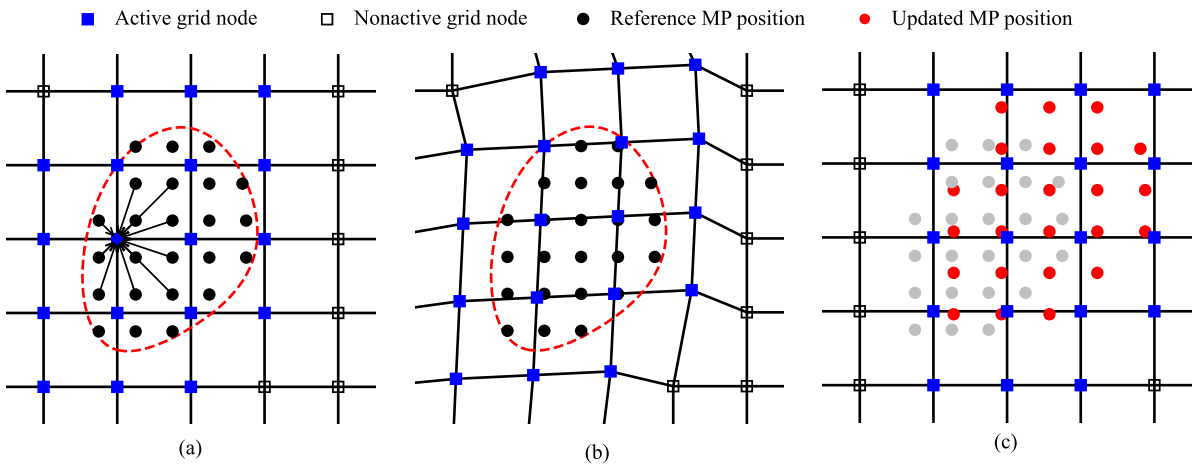

Fig. 2. Illustration of a computational cycle for the MPM: (a) MPM integration phase, (b) MPM solution phase, and (c) MPM convection phase.

particles (*i.e.*, material points). As a simple illustration, Fig. 2 displays a typical MPM computational cycle for a representative problem with a reference configuration domain Ω_0 at time t (see Fig. 2(a)) and a current configuration domain Ω at time $t + \Delta t$ (see Fig. 2(c)). In the standard MPM, the material points directly contribute to the internal force calculation at the nodes of the grid cell in which material points are located. As C^0 continuous linear shape functions are used, the discontinuity in the shape function gradient can cause the so-called "cell crossing issue" when material points move from one grid cell to another. As a consequence, the cell crossing issue can lead to huge oscillations in both the nodal internal forces and stresses, which can therefore influence the accuracy and numerical stability of MPM, see for example González Acosta et al. (2020) and Zheng (2022). To remedy this cell crossing issue, we consider the Generalized Interpolation Material Point (GIMP) method (Bardenhagen and Kober, 2004), in which the shape functions are constructed by integrating linear FEM shape functions over the MP support domain Ω_{mp} (with its length being $2l_{mp}$ in the one-dimensional case). As an extension of the linear shape functions, the GIMP shape functions $S_{i,mp}$ are C^1 continuous, which can be written for the 1D case as

$$S_{i,mp}\left(x_{mp}\right)=\begin{cases}\dfrac{\left(h+l_{mp}+x_{mp}-x_i\right)^2}{4hl_{mp}}, & -h-l_{mp}<x_{mp}-x_i\le -h+l_{mp},\\ 1+\dfrac{x_{mp}-x_i}{h}, & -h+l_{mp}<x_{mp}-x_i\le -l_{mp},\\ 1-\dfrac{\left(x_{mp}-x_i\right)^2+l_{mp}^2}{2hl_{mp}}, & -l_{mp}<x_{mp}-x_i\le l_{mp},\\ 1-\dfrac{x_{mp}-x_i}{h}, & l_{mp}<x_{mp}-x_i\le h-l_{mp},\\ \dfrac{\left(h+l_{mp}-x_{mp}+x_i\right)^2}{4hl_{mp}}, & h-l_{mp}<x_{mp}-x_i\le h+l_{mp},\end{cases} \tag{11}$$

where x_{mp} and x_i are the positions of material points and nodes of the grid cell, subscripts mp and i respectively denote the mp^{th} material point and the ith grid cell node, h is the grid cell size, and l_{mp} is the half length of the support domain of the material point. More details regarding the GIMP method are given in Bardenhagen and Kober (2004) and are therefore not included in this study.

By applying the principle of virtual work, the weak version of the momentum balance equation is obtained by standard manipulation of the governing equations and boundary conditions as

$$\int_{\Omega}\delta\boldsymbol{v}^{\mathrm{T}}\rho\boldsymbol{a}\mathrm{d}\Omega=\int_{\Omega}\delta\boldsymbol{v}^{\mathrm{T}}\cdot(\nabla\cdot\boldsymbol{\sigma})\mathrm{d}\Omega+\int_{\Omega}\delta\boldsymbol{v}^{\mathrm{T}}\cdot\rho\boldsymbol{b}\mathrm{d}\Omega+\int_{\Gamma_\tau}\delta\boldsymbol{v}^{\mathrm{T}}\cdot\bar{\boldsymbol{\tau}}\mathrm{d}\Gamma_\tau, \tag{12}$$

where $\delta\boldsymbol{v}$ is a vector of suitable test functions, $\boldsymbol{a}$ is the soil particle acceleration, Ω is the current problem domain, Γ_τ is the boundary surface, and $\bar{\boldsymbol{\tau}}$ is the surface traction force vector, which is obtained by interpolation from finite volume cells to material points and calculated using Eq. (10).

After performing spatial approximation using the GIMP shape functions Eq. (11), the weak formulation of the momentum balance Eq. (12) can be further expressed using the discrete version:

$$\mathbf{m}\hat{\boldsymbol{a}}=\boldsymbol{f}^{trac}+\boldsymbol{f}^{body}-\boldsymbol{f}^{int}, \tag{13}$$

where $\mathbf{m}$ is the global mass matrix which is diagonalized through "mass lumping" (more details can be found in Zheng et al. (2021)), $\hat{\boldsymbol{a}}$ is the nodal acceleration of the soil, and $\boldsymbol{f}^{trac}$, $\boldsymbol{f}^{body}$, and $\boldsymbol{f}^{int}$ are nodal force vectors related to the surface traction, body force and internal force, respectively. Note that, in the framework of GIMP, the mass matrix and force vectors in the discrete version of the governing equation (Eq. (13)) for a specific grid cell node i are defined as

$$\mathbf{m}_i=\sum_{mp=1}^{N_{mp}}\boldsymbol{S}_{ip}^{\mathrm{T}}\left(\boldsymbol{x}_{mp}\right)\rho V_{mp}\boldsymbol{S}_{ip}\left(\boldsymbol{x}_{mp}\right), \tag{14}$$

$$\boldsymbol{f}_i^{trac}=\sum_{mp=1}^{N_{bmp}}\boldsymbol{S}_{ip}^{\mathrm{T}}\left(\boldsymbol{x}_{mp}\right)\bar{\boldsymbol{\tau}}, \tag{15}$$

$$\boldsymbol{f}_i^{body}=\sum_{mp=1}^{N_{mp}}\boldsymbol{S}_{ip}^{\mathrm{T}}\left(\boldsymbol{x}_{mp}\right)\rho V_{mp}\boldsymbol{b}, \tag{16}$$

$$\boldsymbol{f}_i^{int}=\sum_{mp=1}^{N_{mp}}\boldsymbol{B}_{ip}^{\mathrm{T}}\left(\boldsymbol{x}_{mp}\right)V_{mp}\boldsymbol{\sigma}, \tag{17}$$

where N_{mp} is the total number of material points, $\boldsymbol{x}_{mp}$ and V_{mp} are respectively the coordinates and volume of the mp^{th} material point, N_{bmp} is the total number of nodes on which the external force is applied, and the strain–displacement matrices $\boldsymbol{B}_{ip}$ contain derivatives of the shape functions $\boldsymbol{S}_{ip}$. It is worth noting that, since undrained seabed deformations are considered in this study, a total stress analysis is performed to simulate large dynamic deformations in the topography.

An explicit time stepping scheme is adopted for the integration of the discrete version of the governing equation (Eq. (13)). For computational convenience, a lumped mass matrix using a row summation technique is used. Considering a representative step at a generic time t_n, the acceleration at node i can be calculated as

$$\hat{\boldsymbol{a}}_i^{t_n}=\mathbf{m}^{-1}\left(\boldsymbol{f}^{trac}+\boldsymbol{f}^{body}-\boldsymbol{f}^{int}\right), \tag{18}$$

$$\hat{\boldsymbol{v}}_i^{t_n+\Delta t_n}=\mathbf{m}^{-1}\left(\sum_{mp=1}^{n_{mp}}\boldsymbol{S}_{ip}^{\mathrm{T}}\left(\boldsymbol{x}_{mp}\right)\rho V_{mp}\boldsymbol{v}_{mp}^{t_n}+\Delta t_n\left(\boldsymbol{f}^{trac}+\boldsymbol{f}^{body}-\boldsymbol{f}^{int}\right)\right), \tag{19}$$

and the state variables for a material point mp are updated as follows:

$$\boldsymbol{v}_{mp}^{t_n+\Delta t_n} = \boldsymbol{v}_{mp}^{t_n} + \Delta t_n \sum_{i=1}^{N_n} S_{ip}\left(\boldsymbol{x}_{mp}\right) \hat{\boldsymbol{a}}_i^{t_n}, \tag{20}$$

$$\boldsymbol{x}_{mp}^{t_n+\Delta t_n} = \boldsymbol{x}_{mp}^{t_n} + \Delta t_n \sum_{i=1}^{N_n} S_{ip}\left(\boldsymbol{x}_{mp}\right) \hat{\boldsymbol{v}}_i^{t_n+\Delta t_n}, \tag{21}$$

where N_n is the total number of nodes in the problem domain, and Δt_n is the time step increment for the nth computational step. Using the updated nodal velocity at grid cell nodes in Eq. (19), the strain and stress rates at material point positions are updated using Eqs. (5) and (6). After calculating all the state variables at the material point positions, the computational cycle is completed and a new cycle following the same procedure starts.

Notice that, since an explicit time integration scheme has been adopted for the MPM, the time step size Δt is required to be smaller than the critical value defined by the well-known Courant–Friedrichs–Lewy (CFL) condition for achieving a stabilized numerical solution. In the MPM framework, the critical time step size Δt^{crit} is given by

$$\Delta t^{crit} = \frac{h}{\sqrt{(K+4G/3)/\rho}}, \tag{22}$$

where h is the background grid cell size, and K and G are the bulk and shear moduli, respectively. In this study, following ideas reported in de Vaucorbeil et al. (2020) and Wyser et al. (2020), an adaptive time step Δt_n^1 that takes the velocities of material points into consideration is employed:

$$\Delta t_n^s = \alpha \frac{h}{\sqrt{(K+4G/3)/\rho} + \max(|v_x|, |v_y|)}, \tag{23}$$

where α is the time step multiplier, v_x and v_y are the velocity components of material points in the horizontal and vertical directions, and $\max(|v_x|, |v_y|)$ is the maximum value of the velocity components of all material points. More details can be found in de Vaucorbeil et al. (2020) and Wyser et al. (2020).

In a similar manner to low-order FEMs, the accuracy of the GIMP may also be negatively impacted by volumetric locking when the soil deforms at (nearly) constant volume (*e.g.*, during plastic deformation) and a full strain integration is adopted in the stress analysis (Coombs et al., 2018). Different numerical algorithms, such as mixed variational principles (Mast et al., 2012; Iaconeta et al., 2019), fractional time stepping (Kularathna and Soga, 2017; Zhang et al., 2017), and $\overline{\mathrm{F}}$ and $\overline{\mathrm{B}}$ methods (Coombs et al., 2018; Bisht et al., 2021; Yuan et al., 2021a), have already proven successful against locking in large-deformation problems. The $\overline{\mathrm{B}}$ method within the framework of GIMP, which was recently adopted by Zheng et al. (2022), is therefore implemented in the proposed hybrid material point/finite volume method for the simulation of large dynamic elastoplastic deformation of the soil seabed.

3.2. Finite volume method for shallow water flows

To solve the nonlinear shallow water equations for the free-surface flows, we implement a finite volume method of the Roe type using non-uniform grids to avoid interpolation procedures at the interface. Similar techniques have been studied in Arvanitis and Delis (2006) and Al-Ghosoun (2021) for shallow water equations. Thus, Eqs. (9) are rewritten in a conservative form as

$$\frac{\partial \boldsymbol{U}}{\partial t} + \frac{\partial \mathbf{F}(\boldsymbol{U})}{\partial x} = \mathbf{Q}(\boldsymbol{U}) + \mathbf{S}(\boldsymbol{U}), \tag{24}$$

where

$$\boldsymbol{U} = \begin{pmatrix} h \\ hv \end{pmatrix}, \quad \mathbf{F}(\boldsymbol{U}) = \begin{pmatrix} hv \\ hv^2 + \frac{1}{2}gh^2 \end{pmatrix},$$

$$\mathbf{Q}(\boldsymbol{U}) = \begin{pmatrix} 0 \\ -gh\dfrac{\partial B}{\partial x} \end{pmatrix}, \quad \mathbf{S}(\boldsymbol{U}) = \begin{pmatrix} 0 \\ -gM_b^2 h \dfrac{v|v|}{h^{\frac{4}{3}}} \end{pmatrix}.$$

To integrate the system (24) in time we divide the time interval into sub-intervals $[t_n, t_{n+1}]$ with variable size Δt_n, such that $t_n = t_{n-1} + \Delta t_n$, $n = 1, 2, \ldots$ and $t_0 = 0$. For simplicity in the presentation, we use the notation $\boldsymbol{U}^n(x)$ to denote the discrete solution $\boldsymbol{U}(t_n, x)$ at time $t = t_n$. To deal with the differential source term $\mathbf{Q}(\boldsymbol{U})$ and the non-differential source term $\mathbf{S}(\boldsymbol{U})$ in (24), we consider the splitting operator introduced in Strang (1968), which consists of two consecutive steps as follows:

Step 1: Solve for $\widetilde{\boldsymbol{U}}$

$$\frac{\widetilde{\boldsymbol{U}} - \boldsymbol{U}^n}{\Delta t_n} + \frac{\partial \mathbf{F}(\boldsymbol{U}^n)}{\partial x} = \mathbf{Q}\left(\boldsymbol{U}^n\right). \tag{25}$$

Step 2: Solve for $\boldsymbol{U}^{n+1}$

$$\frac{\boldsymbol{U}^{n+1} - \widetilde{\boldsymbol{U}}}{\Delta t_n} = \mathbf{S}\left(\widetilde{\boldsymbol{U}}\right). \tag{26}$$

For the space discretization of systems (Eqs. (25) and (26)), we discretize the space domain into non-uniform control volumes $\left[x_{i-\frac{1}{2}}, x_{i+\frac{1}{2}}\right]$ of length Δx_i, and we also use the notation $\boldsymbol{U}_i^n$ to denote the space-averaged approximation of $\boldsymbol{U} = \boldsymbol{U}(t, x)$ in the cell $\left[x_{i-\frac{1}{2}}, x_{i+\frac{1}{2}}\right]$ at time t_n and $\boldsymbol{U}_{i+\frac{1}{2}}^n$ to denote the intermediate solution at $x_{i+\frac{1}{2}}$ at time t_n:

$$\boldsymbol{U}_i^n = \frac{1}{\Delta x_i} \int_{x_{i-\frac{1}{2}}}^{x_{i+\frac{1}{2}}} \boldsymbol{U}(t_n, x)\, dx, \qquad \boldsymbol{U}_{i+\frac{1}{2}}^n = \boldsymbol{U}\left(t_n, x_{i+\frac{1}{2}}\right). \tag{27}$$

Hence, integrating the system Eq. (25) over the space–time control domain $\left[x_{i-\frac{1}{2}}, x_{i+\frac{1}{2}}\right] \times \left[t_n, t_{n+1}\right]$, yields the following fully-discrete system:

$$\boldsymbol{U}_i^{n+1} = \boldsymbol{U}_i - \frac{\Delta t_n}{\Delta x_i}\left(\mathbf{F}_{i+\frac{1}{2}}^n - \mathbf{F}_{i-\frac{1}{2}}^n\right) + \Delta t_n \mathbf{Q}_i^n, \tag{28}$$

where $\mathbf{F}_{i\pm\frac{1}{2}}^n = \mathbf{F}\left(\boldsymbol{U}_{i\pm\frac{1}{2}}^n\right)$ are the numerical fluxes at $x = x_{i\pm\frac{1}{2}}$ and time $t = t_n$, and $\mathbf{Q}_i^n$ is the space-averaged source term defined as

$$\mathbf{Q}_i^n = \frac{1}{\Delta x_i} \int_{x_i-\frac{1}{2}}^{x_i+\frac{1}{2}} \mathbf{Q}(\boldsymbol{U})\, d\boldsymbol{x}. \tag{29}$$

For the reconstruction of numerical fluxes $\mathbf{F}_{i\pm1/2}^n$ in Eq. (28) in the current work, we consider the well-established Roe reconstruction defined as (Roe, 1981)

$$\mathbf{F}_{i+\frac{1}{2}}^n = \frac{1}{2}\left(\mathbf{F}(\widehat{\boldsymbol{U}}_{i+1}^n) + \mathbf{F}(\widehat{\boldsymbol{U}}_i^n)\right) + \frac{1}{2}\mathbf{A}\left(\widehat{\boldsymbol{U}}_{i+\frac{1}{2}}^n\right)\left(\widehat{\boldsymbol{U}}_i^n - \widehat{\boldsymbol{U}}_{i+1}^n\right), \tag{30}$$

where the averaged states $\widehat{\boldsymbol{U}}_{i+\frac{1}{2}}^n$ are evaluated as

$$\widehat{\boldsymbol{U}}_{i+\frac{1}{2}}^n = \begin{pmatrix} \dfrac{h_i^n + h_{i+1}^n}{2} \\ \dfrac{\sqrt{h_i^n}v_i^n + \sqrt{h_{i+1}^n}v_{i+1}^n}{\sqrt{h_i^n + h_{i+1}^n}} \end{pmatrix}, \tag{31}$$

and the Roe matrix in Eq. (30) is given by $\mathbf{A} = \mathbf{R}\boldsymbol{\Lambda}\mathbf{R}^{-1}$, with

$$\mathbf{R} = \begin{pmatrix} 1 & 1 \\ \widehat{\lambda}_1 & \widehat{\lambda}_2 \end{pmatrix}, \qquad \boldsymbol{\Lambda} = \begin{pmatrix} \widehat{\lambda}_1 & 0 \\ 0 & \widehat{\lambda}_2 \end{pmatrix}, \tag{32}$$

where $\widehat{\lambda}_1 = \widehat{v} - \sqrt{g\widehat{h}}$ and $\widehat{\lambda}_2 = \widehat{v} + \sqrt{g\widehat{h}}$ are the two eigenvalues associated with the system calculated at the averaged state Eq. (31). Note that other finite volume methods developed in the literature for solving hyperbolic systems of conservation laws can also be implemented in our approach without any major conceptual modifications.

Algorithm 1: Coupled solution algorithm for the proposed hybrid material point/finite volume method

Initialize all variables
while $t_n \le T$ **do**
  /* ==========MPM solution cycle========== */
  /* ----------MPM integration phase---------- */
  for *Each material point mp* **do**
    Mapping state variables from material points to grid cell nodes;
    Calculate nodal mass matrix $\mathbf{m}$ and force vectors $\boldsymbol{f}^{trac}$, $\boldsymbol{f}^{body}$, and $\boldsymbol{f}^{int}$ using Eqs. (14) - (17)
  end
  /* ----------MPM solution phase---------- */
  for *Each grid cell node i* **do**
    Evaluate nodal acceleration $\hat{\boldsymbol{a}}_i^{t_n}$ using Eq. (18);
    Update nodal velocity $\hat{\boldsymbol{v}}_i^{t_n+\Delta t_n}$ of grid cell using Eq. (19)
  end
  /* ----------MPM convection phase---------- */
  for *Each material point mp* **do**
    Map state variables from grid cell nodes to material points;
    Update velocities $\boldsymbol{v}_{mp}^{t_n+\Delta t_n}$ and positions $\boldsymbol{x}_{mp}^{t_n+\Delta t_n}$ of material points using Eqs. (20) - (21);
    Calculate strain $\dot{\boldsymbol{\epsilon}}$ (Eq. (5)) and stress $\dot{\boldsymbol{\sigma}}$ (Eq. (6)) rates with the updated nodal velocities $\hat{\boldsymbol{v}}_i^{t_n+\Delta t_n}$
  end
  /* ==========FVM solution cycle========== */
  Reconstruct the bed $B\left(t_n, x\right)$ using a cubic interpolation from the material point positions $\boldsymbol{x}_{mp}^{t_n+\Delta t_n}$ to finite volume cells
  /* ----------Solving the shallow water equations---------- */
  for *Each finite control volume* $\left[x_{i-\frac{1}{2}}, x_{i+\frac{1}{2}}\right]$ **do**
    Compute the numerical fluxes
  end
  Compute the vertical force p using hydrostatic pressure and horizontal force τ_f using bed friction;
  Interpolate forces p and τ_f from finite volume cells to material points at the interface and determine surface traction force vector $\tilde{\boldsymbol{\tau}}$;
  Determine the time step size Δt_n for hybrid material point/finite volume method using Eq. (38) and update total computational time by $t_n = t_n + \Delta t_n$
end

For the discretization of the source term $\mathbf{Q}_i^n$, we use a well-balanced reconstruction investigated in Arvanitis and Delis (2006) and Al-Ghosoun (2021). This property is achieved in our implementation by splitting the integral in Eq. (29) over the two sub-cells $\left[x_{i-\frac{1}{2}}, x_i\right]$ and $\left[x_i, x_{i+\frac{1}{2}}\right]$ of the control volume $\left[x_{i-\frac{1}{2}}, x_{i+\frac{1}{2}}\right]$ as

$$\mathbf{Q}_i^n = \frac{1}{\Delta x_i}\left(\frac{(x_i - x_{i-1})}{2}\mathbf{Q}^L_{i-\frac{1}{2}} + \frac{(x_{i+1} - x_i)}{2}\mathbf{Q}^R_{i+\frac{1}{2}}\right), \tag{33}$$

where $\mathbf{Q}^L_{i-\frac{1}{2}}$ and $\mathbf{Q}^R_{i+\frac{1}{2}}$ are the space-averaged approximations of $\mathbf{Q}$ in the sub-cells $\left[x_{i-\frac{1}{2}}, x_i\right]$ and $\left[x_i, x_{i+\frac{1}{2}}\right]$, defined by

$$\begin{aligned}\mathbf{Q}^L_{i-\frac{1}{2}} &= \begin{pmatrix} 0 \\ -g\dfrac{h_i + h_{i-1}}{2}\left(B_i - B_{i-1}\right) \end{pmatrix}, \\ \mathbf{Q}^R_{i-\frac{1}{2}} &= \begin{pmatrix} 0 \\ -g\dfrac{h_{i+1} + h_i}{2}\left(B_{i+1} - B_i\right) \end{pmatrix}. \end{aligned} \tag{34}$$

It is expected that, for small values of the water depth h, the bed friction term dominates other terms in the momentum equation. This is due to the presence of the term $h^{\frac{4}{3}}$ in the denominator of τ_f in Eq. (8). To resolve this challenge in our method we implement a semi-implicit scheme for the time integration of the source term $\mathbf{S}$ in Eq. (26) as

$$\begin{aligned}\frac{h^{n+1} - \widetilde{h}}{\Delta t_n} &= 0, \\ \frac{(hv)^{n+1} - \left(\widetilde{h}\widetilde{v}\right)}{\Delta t_n} &= -gM_b^2\frac{(hv)^{n+1}\left|\widetilde{v}\right|}{\left(\widetilde{h}\right)^{\frac{4}{3}}}, \end{aligned} \tag{35}$$

where $\widetilde{h}$ and $\widetilde{v}$ are the water height and velocity obtained from the first step Eq. (25) of the splitting procedure. It is easy to verify that by solving the second equation in Eq. (35) for $(hv)^{n+1}$ we obtain

$$(hv)^{n+1} = \frac{\left(\widetilde{h}\widetilde{v}\right)}{1 + \Delta t_n g M_b^2\left|\widetilde{v}\right| / \left(\widetilde{h}\right)^{\frac{4}{3}}}. \tag{36}$$

Since the above time integration scheme is explicit, the considered finite volume method is conditionally stable, with the selection of time steps being subject to the Courant–Friedrichs–Lewy (CFL) condition. Here, the Courant number C_r is fixed to a given value and Δt_n^w is chosen at each time step according to the CFL condition

$$\Delta t_n^w = C_r\frac{\min\left(\Delta x_i\right)}{\max\left(\left|\hat{\lambda}_1^+\right|, \left|\hat{\lambda}_1^-\right|, \left|\hat{\lambda}_2^+\right|, \left|\hat{\lambda}_2^-\right|\right)}, \tag{37}$$

where $\hat{\lambda}_1^{\pm} = \hat{v}_1^{\pm} - \sqrt{g\hat{h}_1^{\pm}}$ and $\hat{\lambda}_2^{\pm} = \hat{v}_2^{\pm} + \sqrt{g\hat{h}_2^{\pm}}$, in which $\hat{h}_{1,2}^{\pm}$ and $\hat{v}_{1,2}^{\pm}$ are computed using the space-averaged solutions in the control volume $\left[x_{i-\frac{1}{2}}, x_{i+\frac{1}{2}}\right]$ and its two neighbouring cells as

$$\hat{h}_1^+ = \frac{h_{i+1} + h_i}{2}, \qquad \hat{h}_1^- = \frac{h_i + h_{i-1}}{2}, \qquad \hat{v}_1^+ = \frac{\sqrt{h_{i+1}}v_{i+1} + \sqrt{h_i}v_i}{\sqrt{h_{i+1}} + \sqrt{h_i}},$$

$$\hat{v}_2^+ = \frac{\sqrt{h_i}v_i + \sqrt{h_{i-1}}v_{i-1}}{\sqrt{h_i} + \sqrt{h_{i-1}}}.$$

It is evident that the finite volume reconstruction given in Eq. (28) is only first-order accurate, but in the current study we adapt flux limiters to reconstruct a second-order accurate finite volume method for solving Eq. (24). Details on the implementation of this method for solving the shallow water Eqs. (9) can be found in Benkhaldoun et al. (2012) and they are omitted here. It should also be pointed out that, as explicit time integration schemes are used in both MPM and FVM, the adopted time step size Δt_n at the nth computational step for the hybrid material point/finite volume method is adjusted as

$$\Delta t_n = \min\left(\Delta t_n^s, \Delta t_n^{tv}\right), \tag{38}$$

where Δt_n^s and Δt_n^{tv} are the time steps given by Eqs. (23) and (37), respectively. Finally, details regarding the coupled solution algorithm for the hybrid material point/finite volume method are summarized in Algorithm 1.

4. Numerical results and examples

This section presents the results of several verification examples to support the numerical performance of the MPM for reproducing the elastoplastic large deformations and the FVM for capturing the shallow water flows. We also consider two numerical examples to separately validate the suitability of the MPM and FVM for solving large deformations and shallow water waves, respectively. The excellent numerical capability of the proposed hybrid material point/finite volume method, for the numerical simulation of shallow waves caused by large dynamic deformations of seabeds, is demonstrated through two typical applications. We consider the problem of an undrained clay column collapse in a water body at rest and the problem of a clay column collapse in a dam-break flow. In all our simulations, unless stated otherwise, the water density $\rho = 1000\,\mathrm{kg/m^3}$, the gravitational acceleration $g = 9.81\,\mathrm{m/s^2}$, and the Manning coefficient $M_b = 0.0015\,\mathrm{s/m^{1/3}}$. In addition, in the computations reported in this section, the Courant number is set to $C_r = 0.75$ and the time step size Δt_n is adjusted at each time step according to the CFL stability condition as Eqs. (23), (37), and (38). It should be emphasized that, at each time step, the large deformation in the bed yields changes in the water depth and flow velocity, which consequently affects the calculation of the eigenvalues in Eq. (37). Hence, the effect of bed deformation is also implicitly accounted for in updating the time step, which involves the variation of water depth and the flow velocity in the horizontal direction resulting from the deformation.

4.1. Accuracy of MPM for the dynamic collapse of a tunnel face

As a preliminary verification of the excellent performance of the GIMP for large dynamic deformation problems, the two-dimensional elastoplastic collapse of a tunnel face is first studied. Such a benchmark problem has previously been investigated by experimental study (Matsuo et al., 2016) and the well-established SPH method (Matsuo et al., 2016; Feng et al., 2021). Fig. 3 shows the plane strain numerical model for the tunnel face, including the associated geometry and boundary conditions. To enable a fair comparison, the problem geometries and material properties of the tunnel face collapse model are chosen to be exactly the same as those adopted by Matsuo et al. (2016) and are listed in Table 1. The lining structure constructed at the tunnel roof is considered to be rigid, while an open-face condition is assumed with zero face pressure. The boundaries are assumed to be non-slip for the base and tunnel roof (lining structure), while free-slip conditions are enforced at the two lateral boundaries. Within the framework of MPM, the problem domain is discretized by 4-node quadrilateral grid cells of size $0.01\,\mathrm{m} \times 0.01\,\mathrm{m}$.

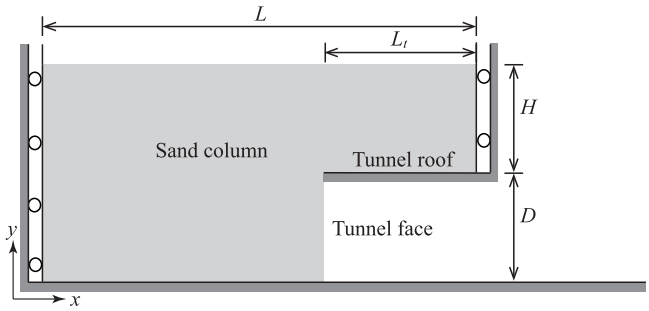

Fig. 3. Geometry and boundary conditions used for the problem of elastoplastic tunnel face collapse.

Table 1
Problem geometries and material properties for analyzing the problem of elasto-plastic tunnel face collapse.

Problem geometries			Material properties		
Total length	L	42 cm	Young's modulus	E	5.84 MPa
Tunnel length	L_t	12 cm	Poisson's ratio	ν	0.3
Tunnel overburden	H	8 cm	Soil unit weight	γ	21.7 kN/m^3
Tunnel height	D	8 cm	Friction angle	ϕ	21.9 $^\circ$
Overburden ratio	H/D	1.0	Cohesion	c	0 kPa

Fig. 4 shows a comparison of the final configuration of the collapsed tunnel face between the GIMP simulation and experiment data. The coloured MPs respectively indicate the final total displacement and vertical stress, and the solid lines with open squares indicate the final experimental free-surface from Matsuo et al. (2016). It can be clearly observed that the experimental post-failure patterns of the tunnel face, including the free-surface profile, ground settlement and large soil run-out distance, are well captured by the GIMP. Meanwhile, the numerical solutions obtained using the GIMP also compare quite well with the solutions obtained using the SPH method in Feng et al. (2021), which are not included here for reasons of brevity. It should be mentioned that slight stress oscillations are visible in the vertical stress solutions, which are directly attributed to the substantial relocation of MPs occurring during the large deformations. This relocation, along with the simple MP support domain updating algorithm adopted in this study, would lead to discontinuous or overlapping support domains of MPs (as discussed in Charlton, 2018), which yield visible stress oscillations (which are not caused by cell crossing). More advanced support domain updating algorithms proposed in recent studies (Sadeghirad et al., 2011; Charlton, 2018; Coombs et al., 2020) are expected to positively impact stress recovery calculations and will be investigated in a future study.

To clearly show the dynamic collapse process of the tunnel face, Fig. 5 provides the evolution of the total velocity field $v_{tot} = \sqrt{v_x^2 + v_y^2}$ for MPs at four different time instants, namely $t = 0\,\mathrm{s}$, $0.1\,\mathrm{s}$, $0.2\,\mathrm{s}$ and $1.0\,\mathrm{s}$, where v_x and v_y are respectively the velocities of MPs in the horizontal and vertical directions. It can be seen that the dynamic collapse starts from the bottom part of the tunnel face and then gradually propagates to the ground surface, which leads to an overall failure mechanism and thereby to significant surface settlements. In addition, the collapse of the tunnel face is found to mainly concentrate in a local area in the vicinity of the tunnel face. Note that the performance of the considered MPM is very attractive, since the computed solutions remain stable and are highly accurate even though relatively few particles are used in each element.

4.2. Accuracy of FVM for a dam-break flow problem

For the validation of the FVM, we consider a dam-break flow problem over a frictionless flat bottom in the domain $[0, 1.0\,\mathrm{m}]$, which

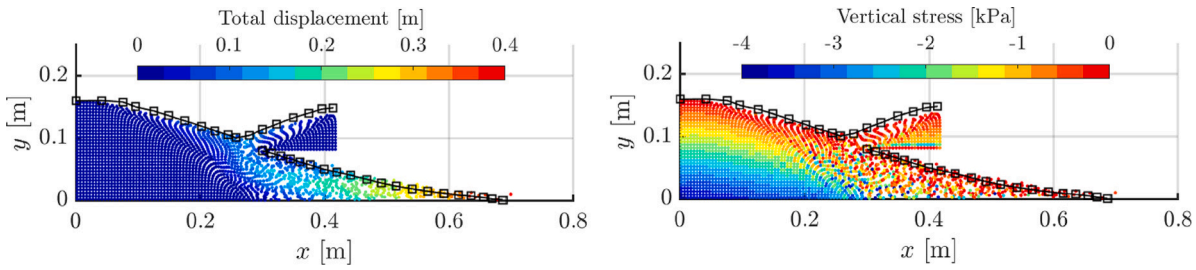

Fig. 4. Comparisons of post-failure configurations obtained using the MPM and experimental results (denoted by solid lines with open squares) for the problem of elasto-plastic tunnel face collapse with $H/D = 1.0$.

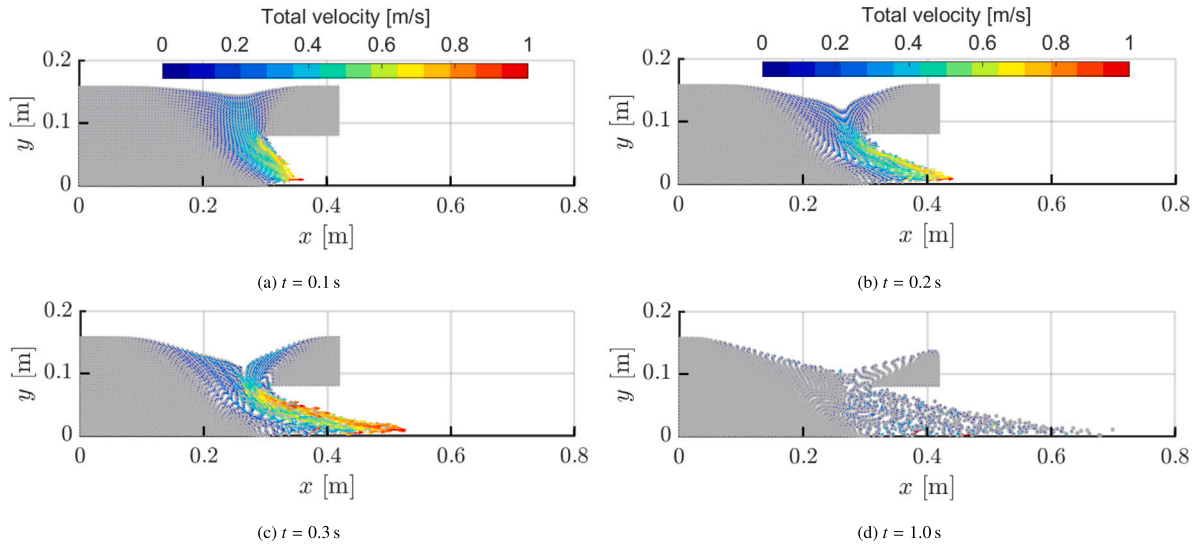

(a) $t = 0.1$ s (b) $t = 0.2$ s

(c) $t = 0.3$ s (d) $t = 1.0$ s

Fig. 5. Time evolution of the total velocity fields v_{tot} at material point positions for the problem of elastoplastic tunnel face collapse.

was previously studied in Aiabadi et al. (2010) and Al-Ghosoun et al. (2021). The considered initial flow conditions are defined as

$$h(x,0) = \begin{cases} 1.0\,\text{m}, & \text{if} \quad x \le 0.5\,\text{m}, \\ 0.5\,\text{m}, & \text{elsewhere}, \end{cases} \qquad u(x,0) = 0\,\text{m/s}.$$

Note that, for this problem, a barrier is located at $x = 0.5$ m to separate the two initial water heights and at time $t = 0$ s the dam break is triggered, which causes a shock wave travelling downstream and a rarefaction wave travelling upstream. The analytical solutions for $h(x,t)$ and $u(x,t)$ (with their units respectively being m and m/s) for this dam-break problem can be derived as (Aiabadi et al., 2010)

$$h(x,t) = \begin{cases} 1.0, & \text{if} \quad x < \frac{1}{2} - t\sqrt{g}, \\ \frac{1}{9g}\left(2\sqrt{g} - \frac{2x-1}{2t}\right)^2, & \text{if} \quad \frac{1}{2} - t\sqrt{g} \le x \le (u_2 - c_2)\,t + \frac{1}{2}, \\ \frac{1}{4}\left(\sqrt{1 + \frac{16C_s^2}{g}} - 1\right), & \text{if} \quad (u_2 - c_2)\,t + \frac{1}{2} < x \le C_s t + \frac{1}{2}, \\ \frac{1}{2}, & \text{if} \quad C_s t + \frac{1}{2} > x, \end{cases}$$

$$u(x,t) = \begin{cases} 0, & \text{if} \quad x < \frac{1}{2} - t\sqrt{g}, \\ \frac{1}{3t}\left(2x - 1 + 2\sqrt{g}\right), & \text{if} \quad \frac{1}{2} - t\sqrt{g} \le x \le (u_2 - c_2)\,t + \frac{1}{2}, \\ u_2, & \text{if} \quad (u_2 - c_2)\,t + \frac{1}{2} < x \le C_s t + \frac{1}{2}, \\ 0, & \text{if} \quad C_s t + \frac{1}{2} > x, \end{cases}$$

where $u_2 = \left(C_s - \frac{g}{8C_s}\left(1 + \sqrt{1 + \frac{16C_s^2}{g}}\right)\right)$ m/s, $c_2 = \left(\sqrt{\frac{g}{4}\left(\sqrt{1 + \frac{16C_s^2}{g}} - 1\right)}\right)$ m/s, and $C_s = 2.9579$ m/s. For comparison, numerical simulations are performed using the adopted FVM solver on both uniform and non-uniform meshes with 50 and 100 control volumes. For the uniform meshes, the spatial step $\Delta x = 0.02$ m and 0.01 m for the meshes with 50 and 100 control volumes, respectively. For the non-uniform meshes, the spatial steps Δx_i are respectively chosen as

$$\Delta x_i = \begin{cases} 0.016\,\text{m}, & \text{if} \quad 0.25\,\text{m} \le x_i \le 0.75\,\text{m}, \\ 0.03\,\text{m}, & \text{elsewhere}, \end{cases} \quad \text{and}$$

$$\Delta x_i = \begin{cases} 0.008\,\text{m}, & \text{if} \quad 0.25\,\text{m} \le x_i \le 0.75\,\text{m}, \\ 0.015\,\text{m}, & \text{elsewhere}. \end{cases}$$

Fig. 6 compares numerical solutions for the water free-surface and velocity at time $t = 0.1$ s using the FVM on uniform and non-uniform meshes. It can be observed that, for both uniform and non-uniform meshes, the accuracy of the numerical results is improved with a refined mesh. The numerical solutions obtained using non-uniform meshes are more accurate than those obtained using their uniform counterparts. For instance, more pronounced numerical diffusion in the shock and rarefaction areas can be seen in the results obtained on uniform meshes than in those obtained using non-uniform meshes. These features are very important when the shallow water equations are solved on non-uniform meshes reconstructed directly from the MPM nodes located on the interface in the coupled model. This would avoid

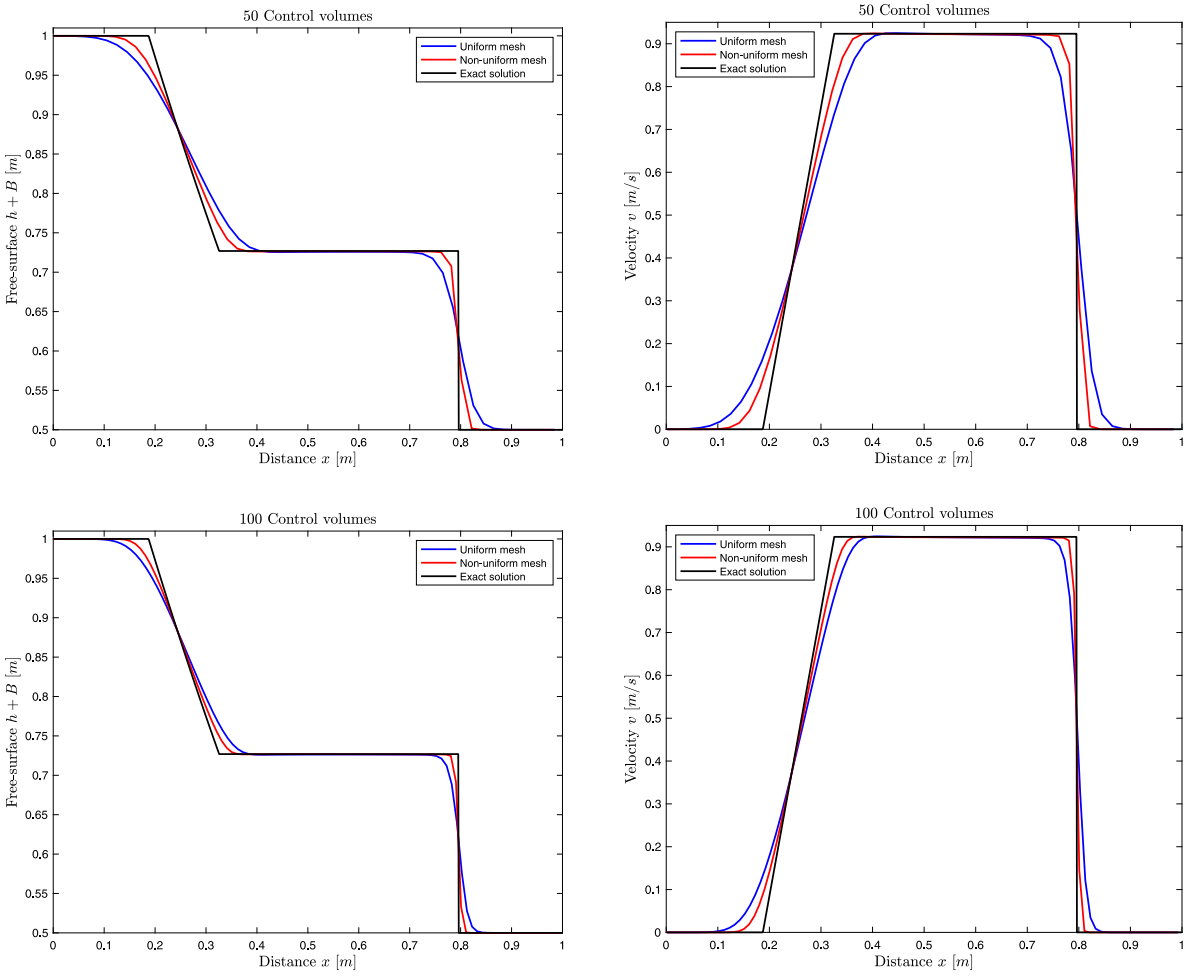

Fig. 6. Results for the water free-surface (first column) and water velocity (second column) obtained at time $t = 0.1$ s using the FVM on uniform and non-uniform meshes with 50 control volumes (first row) and 100 control volumes (second row).

interpolation procedures for matching MPM and FVM nodes on the interface which may introduce extra numerical diffusion in the results obtained for the free-surface solutions.

4.3. Undrained clay column collapse in a body of water at rest

To demonstrate the robustness and capability of the proposed hybrid material point/finite volume method, the shallow water flow caused by the large dynamic collapse of an undrained clay column is studied. The schematic diagram of the considered problem is depicted in Fig. 7. As shown in this figure, the total width of the problem domain is considered to be l. The column has a width of l_0 and a depth of h_0, with its right end being supported by a perfectly rigid wall of zero width at the initial stage of the simulation. The depth between the water free-surface and the bottom of the domain is defined by h_w. The adopted material properties are provided in Table 2 and an initial aspect ratio α (defined by h_0/l_0) of 0.5 is considered, corresponding to a column size of 2.0 m × 1.0 m. The water domain is discretized into 200 control volumes with each having a width of 0.04 m. The grid cell size of the MPM domain is 0.05 m × 0.05 m, which results in 1600 material points for the considered domain. The clay column has a fixed bottom boundary and is supported by rollers on the left lateral boundary. In order to quantify the influence of dynamic collapse of the soil domain on the dynamic propagation of shallow water waves, three different ratios R_{ws} between the water depth h_w and column depth h_0, namely $R_{ws} = 1.0$, 1.5, and 2.0, are investigated.

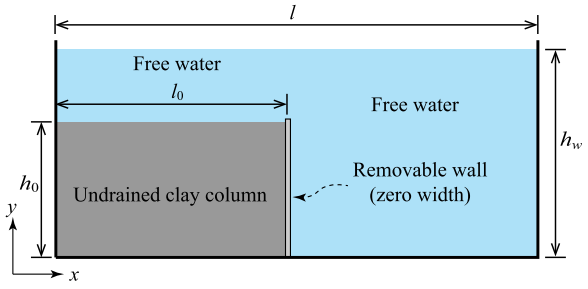

Fig. 7. Schematic diagram for the problem of clay column collapse in a body of water at rest.

Table 2
Domain geometries and material properties for the problem of clay column collapse in a body of water at rest.

Domain geometries			Material properties		
Tank width	l	8.0 m	Young's modulus	E	1000 kPa
Column width	l_0	2.0 m	Poisson's ratio	ν	0.4
Column depth	h_0	1.0 m	Soil unit weight	γ	26.5 kN/m^3
Free water depth	h_w	1.0 m, 1.5 m, 2.0 m	Friction angle	ϕ	0 $^\circ$
			Cohesion	c	3.2 kPa

It should be mentioned that the rigid wall at the column face is simplified as a fully fixed boundary at the initial stage of the simulation

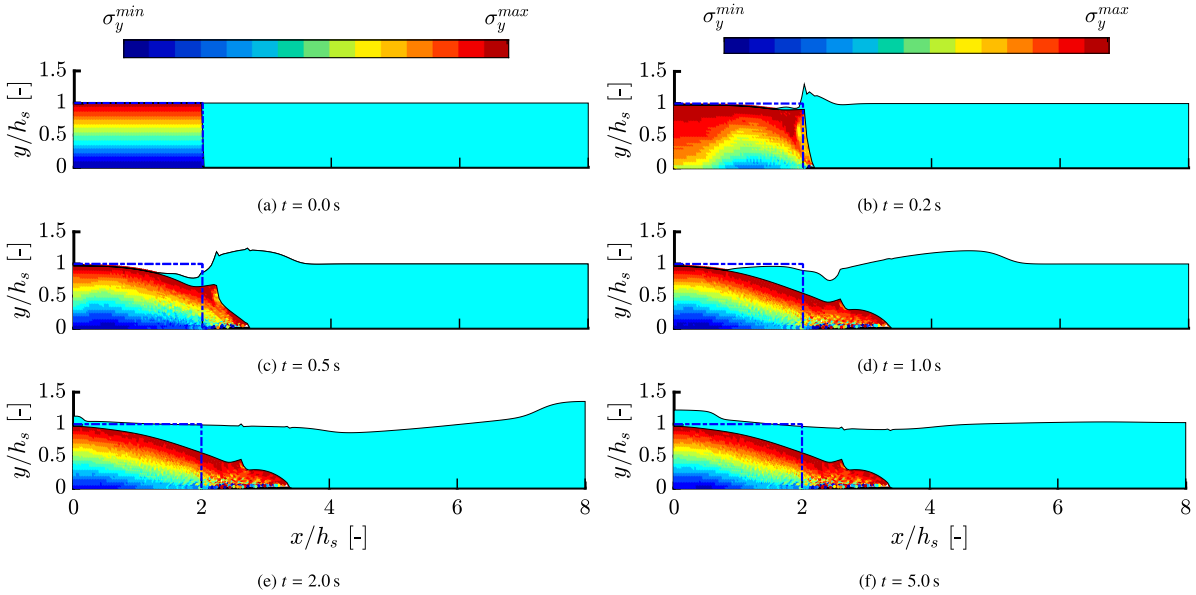

Fig. 8. Time evolution of the vertical stress contours and water free-surface profiles for clay column collapse in a flow at rest with $R_{ws} = 1.0$.

for the purpose of generating the initial quasi-static stress. This fixed boundary is suddenly released at the beginning of the simulation in order to reproduce the sudden removal of the rigid wall. The removal of the rigid wall can lead to a dynamic motion of the soil domain, which results in the change of seabed bathymetry and the flowing of shallow water with the proposed coupled algorithm. The computational domain is assumed to be closed at both the upstream and downstream edges, which allows wave reflections once the water flow reaches the walls.

Fig. 8 depicts the time evolution of the vertical stress (σ_y) contours attached with the MPs and shallow water configurations represented by the FVM solution for the depth ratio $R_{ws} = 1.0$. It can be clearly observed that both the dynamic collapse process of the clay column and the shallow water flow are well captured using the proposed hybrid material point/finite volume method. After the removal of the rigid wall, soil particles gradually move downstream to the right part of tank and experience large deformations. Due to the dynamic response with respect to the rapid deformation of the soil column, a water wave is generated in the local area on the top of the column front face and flows over the deformed seabed. Subsequently, the generated water waves gradually propagate to both ends of the tank. Once the water waves reach the ends, a run-up can be clearly observed. When the simulation undergoes a longer duration, the clay column gradually reaches an equilibrium state, while the water system is expected to stabilize to a steady-state configuration with no further disturbances on the water surface.

As a comparison, Figs. 9 and 10 show the vertical stress contours and water free-surface configurations at four different instants for two values of the ratio $R_{ws} = 1.5$ and 2.0, respectively. As expected, the shallow water wave is again generated in the local area near the column front face due to the dynamic response with respect to the rapid deformation of the column after removal of the rigid wall. From the comparison, it can be concluded that the amplitude of the shallow water wave decreases with an increased value of R_{ws}. However, the final collapsed soil domain does not show a significant difference for the considered values of R_{ws}, which can be related to the fact that the surface friction is quite small, and it shows little influence on the dynamic motion of the soil particles.

In Fig. 11, the changes with time of the water free-surface $\Delta h/h_s$ at two different gauges, $x/h_s = 4$ (domain center) and $x/h_s = 8$ (right end of the tank) are displayed. For both gauges, waves with higher amplitudes on the free-surface are observed for the cases with smaller values of R_{ws}. These results give a clear view of the overall wave patterns and the effect of the bed deformation on the structure of the propagating waves in the upstream and downstream of the domain. In addition to the primary wave, a pair of waves with almost the same amplitudes develop at both sides of the problem domain. As expected, the sudden deformation in the bed generates a wave propagating across the computational domain. The wave splits into several waves and, as time progresses, the waves diminish and the water free-surface becomes flat at the initial height. This confirms the well-balanced property of the proposed finite volume method on non-uniform meshes. It is also important to mention two points concerning the non-uniform control volumes used in the flow simulations. First, there is no need for interpolation procedures to pass the information from one mesh to another in our coupled material point/finite volume method. Second, there is no need to refine the mesh in the finite volume method to resolve the wave fronts, as the material points would generate these refined meshes. Indeed, an important feature of the proposed coupled material point/finite volume method is that it is able to satisfactorily handle procedures using adaptive local grid refinement methods to resolve free-surface wave problems.

To further quantify the results for this problem, we summarize in Table 3 the values obtained for $\Delta s/h_s$, η_{max}/h_s, $|\bar{u}_0|_{max}$ and $|\bar{v}_s|_{max}$ at three different instants using different values of the ratio R_{ws}. Here, Δs is the runoff distance during the collapse of the soil column, η_{max} is the maximum water surface elevation, $|\bar{u}_0|_{max}$ is the maximum value of the dimensionless water velocity $|\bar{u}_0|/\sqrt{gh_s}$, and $|\bar{v}_s|_{max}$ is the maximum value of the dimensionless soil velocity $|\bar{v}_s|/\sqrt{gh_s}$. It is clear that increasing the value of the ratio R_{ws} results in a variation of all considered variables $\Delta s/h_s$, η_{max}/h_s, $|\bar{u}_0|_{max}$ and $|\bar{v}_s|_{max}$ at the three selected instants. The impact of this ratio on the dynamics of both the soil and water is also visible in the obtained results, as seen by comparing the values of $|\bar{u}_0|_{max}$ and $|\bar{v}_s|_{max}$ in Table 3.

4.4. Undrained clay column collapse in a dam-break flow

In this case, the simulation of a clay column collapse in a dam-break flow is investigated using the hybrid material point/finite volume method, and its schematic diagram is shown in Fig. 12. The total width of the tank is defined by l. The clay column has a width of l_0 and a depth of h_0, with its right end being supported by a perfect rigid wall of zero width at the initial stage of the simulation. The initial depths of the

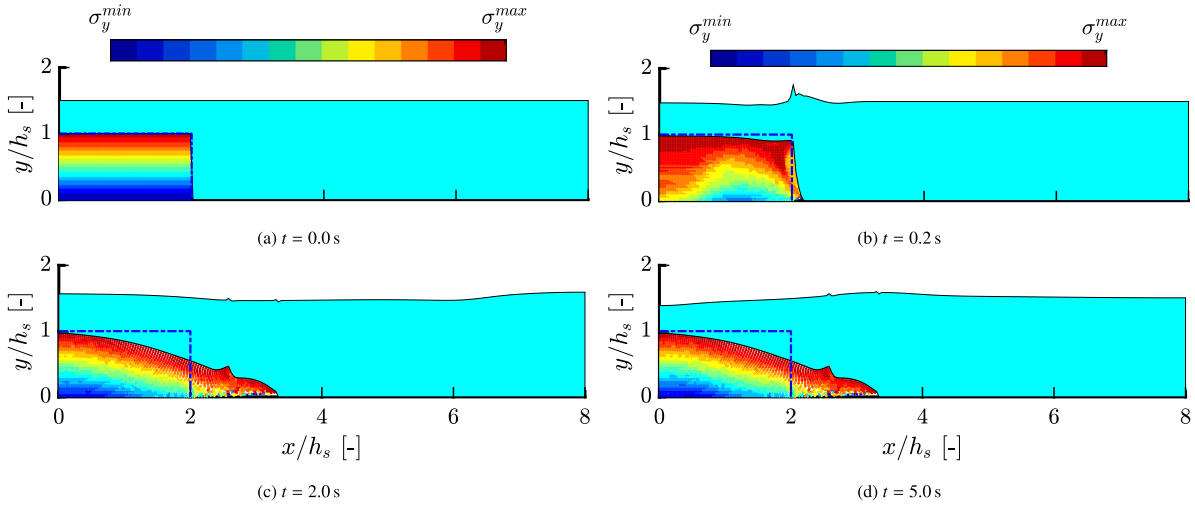

(a) t = 0.0 s (b) t = 0.2 s

(c) t = 2.0 s (d) t = 5.0 s

Fig. 9. Same as Fig. 8 but with R_{ws} = 1.5.

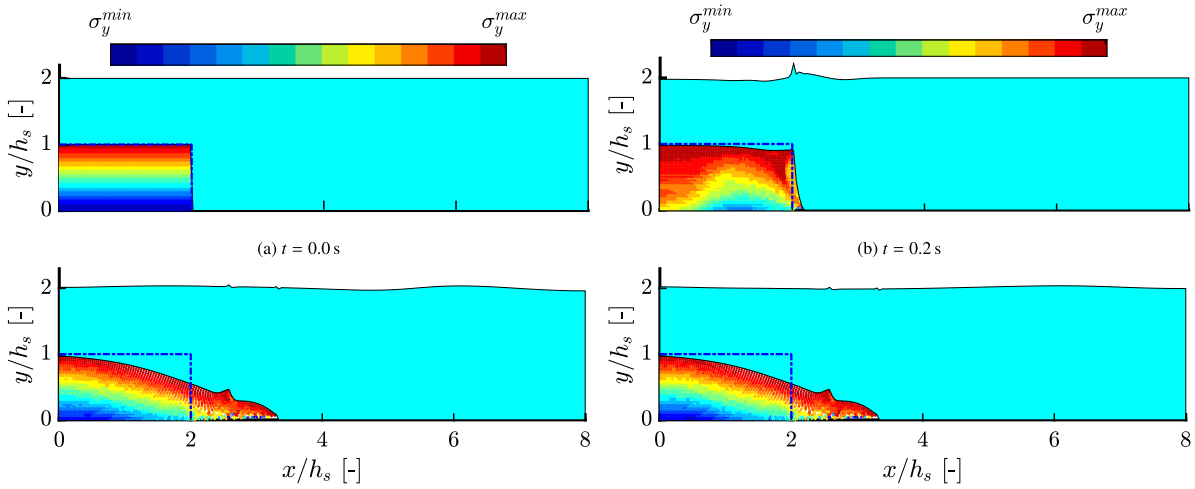

(a) t = 0.0 s (b) t = 0.2 s

(c) t = 2.0 s (d) t = 5.0 s

Fig. 10. Same as Fig. 8 but with R_{ws} = 2.0.

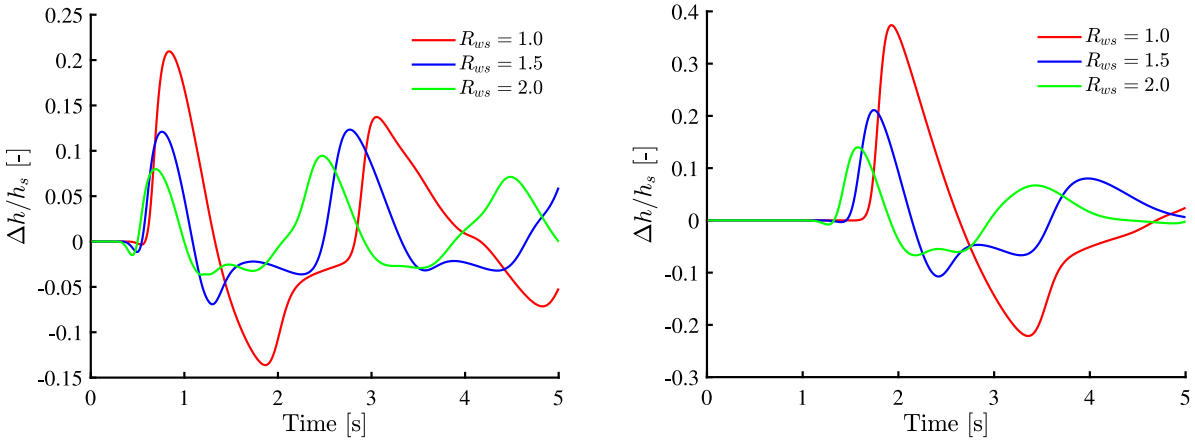

(a) x/h_s = 4.0 (b) x/h_s = 8.0

Fig. 11. Time evolution of water free-surface profiles for the problem of clay column collapse in a body of water at rest at two different gauges, (a) $x/h_s = 4$ and (b) $x/h_s = 8$.

Table 3
Computational results for the undrained clay column collapse in a body of water at rest for different values of R_{ws}.

R_{ws}	$t = 0.5$ s				$t = 1.0$ s				$t = 5.0$ s			
	$\Delta s/h_s$	η_{max}/h_s	$\lvert\bar{v}_s\rvert_{max}$	$\lvert\bar{u}_0\rvert_{max}$	$\Delta s/h_s$	η_{max}/h_s	$\lvert\bar{v}_s\rvert_{max}$	$\lvert\bar{u}_0\rvert_{max}$	$\Delta s/h_s$	η_{max}/h_s	$\lvert\bar{v}_s\rvert_{max}$	$\lvert\bar{u}_0\rvert_{max}$
1.0	0.717	1.245	0.716	0.218	1.344	1.206	0.482	0.197	1.375	1.221	0.044	0.101
1.5	0.681	1.656	0.657	0.107	1.285	1.617	0.549	0.094	1.319	1.601	0.051	0.087
2.0	0.679	2.107	0.654	0.059	1.286	2.076	0.552	0.054	1.319	2.040	0.052	0.030

[a] $\lvert\bar{u}_0\rvert_{max}$ – maximum value of dimensionless water velocity $\lvert\bar{u}_0\rvert/\sqrt{gh_s}$.
[b] $\lvert\bar{v}_s\rvert_{max}$ – maximum value of dimensionless soil velocity $\lvert\bar{v}_s\rvert/\sqrt{gh_s}$.

Table 4
Problem geometries and material properties for the problem of clay column collapse in a dam-break flow.

Problem geometries			Material properties		
Tank width	l	8.0 m	Young's modulus	E	1000 kPa
Column width	l_0	2.0 m	Poisson's ratio	ν	0.4
Column depth	h_0	1.0 m	Soil unit weight	γ	26.5 kN/m^3
Water depths	h_l	0.5 m, 1.0 m, 2.0 m	Friction angle	ϕ	0°
	h_r	1.0 m	Cohesion	c	3.2 kPa

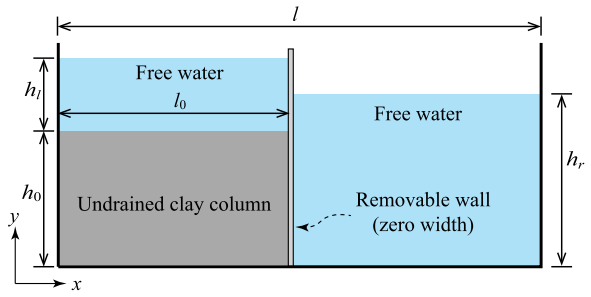

Fig. 12. Schematic diagram for the problem of clay column collapse in a dam-break flow.

water free-surface on the left and right sides of the rigid wall are h_l and h_r, respectively. The water domain is discretized into 200 finite control volumes with each having a width of 0.04 m. The grid cell size of the MPM domain is 0.05 m×0.05 m, which results in 1600 material points for the considered clay domain. The column has a fixed bottom boundary and is supported by rollers on the left lateral boundary. Similarly, three values of R, which is the ratio between the water depths on the left and right sides of the rigid wall, as given by h_l/h_r, are chosen to quantify the influence of a dam-break on the generation and dynamic propagation of shallow water waves. For comparative purposes, the water depth h_r on the right side of wall is considered to be exactly the same as the clay column depth, namely $h_r = h_0$ (see Table 4).

As in the previous numerical example, we present in Fig. 13 the time evolution of vertical stress (σ_y) contours attached with MPs and shallow water configurations represented by the FVM solution, for a depth ratio of $R = 0.5$. The results obtained for $R = 1$ and $R = 2$ are displayed in Figs. 14 and 15, respectively. Unlike the previous clay column collapse in a body of water at rest, the present problem is challenging because the dam-break flow yields complex patterns including shocks, rarefaction waves and hydraulic jumps. It is expected that these flow features have an impact on the soil dynamics. It can be clearly seen from the results obtained that the dynamics of both the dam-break flow and the collapse process of the clay column are well captured using the proposed hybrid material point/finite volume method. For this example, stronger hydraulic jumps are detected for the case with $R = 2$ than for the cases with $R = 1$ and $R = 0.5$. After the dam breaks, soil particles gradually move to the right part of tank and experience large deformations. Obviously, high stresses appear at the bed surface where the bed deformation is taking place. As can be seen, the deformation of the soil column and the dam-break generate rarefaction waves and hydraulic jumps with different crests and troughs propagating along the computational domain. The interaction between these waves generates reflecting waves with different amplitudes in the water free-surface. At a later time, the waves are diminished and the system returns to its initial equilibrium state. Once again, the proposed coupled material point/finite volume method performs well for this test problem, as the deformed bed topography is shown to be accurately resolved using the material point method and the water wave features are well captured using the finite volume method on non-uniform meshes.

Fig. 16 illustrates the changes over time of the water free-surface $\Delta h/h_s$ at two different gauges, $x/h_s = 4$ (domain center) and $x/h_s = 8$ (right-hand end of the tank). Unlike the previous example, the time series in the present case exhibits periodic behaviour with high amplitudes and frequencies. In addition, compared to the previous case, the propagating waves generated by both the dam-break in the water flow and the collapse of the soil column persist longer on the free-surface than those originated by the soil collapse only. It is clear that the total water head experiences high values at the gauge $x/h_s = 8$ located at the downstream of the domain. The coupled material point/finite volume method captures well the periodic features in the water waves at all selected gauges for this example.

A quantification of the results for this problem is carried out and the obtained results for $\Delta s/h_s$, η_{max}/h_s, $\lvert\bar{u}_0\rvert_{max}$ and $\lvert\bar{v}_s\rvert_{max}$ at three different instants using different values of the ratio R are given in Table 5. Here, Δs is the runoff distance during the collapse of the soil column, η_{max} is the maximum water surface elevation, $\lvert\bar{u}_0\rvert_{max}$ is the maximum value of the dimensionless water velocity $\lvert\bar{u}_0\rvert/\sqrt{gh_s}$, and $\lvert\bar{v}_s\rvert_{max}$ is the maximum value of the dimensionless soil velocity $\lvert\bar{v}_s\rvert/\sqrt{gh_s}$. As in the previous example, increasing the value of the ratio R results in a variation of all considered variables $\Delta s/h_s$, η_{max}/h_s, $\lvert\bar{u}_0\rvert_{max}$ and $\lvert\bar{v}_s\rvert_{max}$ at the three selected instants. The impact of this ratio on the dynamics of both the soil and water is also evident in the obtained results, as seen by comparing the values of $\lvert\bar{u}_0\rvert_{max}$ and $\lvert\bar{v}_s\rvert_{max}$ in Table 5. The presented results demonstrate that the proposed computational model is well suited for the prediction of clay column collapse in a dam-break flow. It should be emphasized that the results from the proposed model should be compared with experimental measurements. However, there are no data available until now to carry out this work. Thus, at the moment we can only perform simulations and verify that the results are plausible and consistent.

5. Conclusion

This study has presented a hybrid material point/finite volume method for the numerical simulation of shallow water waves caused by large dynamic deformations in the bathymetry. The governing equations consist of coupling the nonlinear shallow water equations for the water flow and a dynamic elastoplastic system for the seabed deformation. To allow for large deformations under undrained cases, the Drucker–Prager elastoplastic relation is implemented in the present study. The proposed hybrid method is formulated based on a coupling algorithm along the interface of the material point method and finite volume method models, and the coupled scheme is achieved by forces sampled from hydrostatic pressures and surface frictions. It is evident that combining the GIMP shape functions and the $\overline{\mathrm{B}}$ method with a second-order finite volume scheme has proven to produce stable

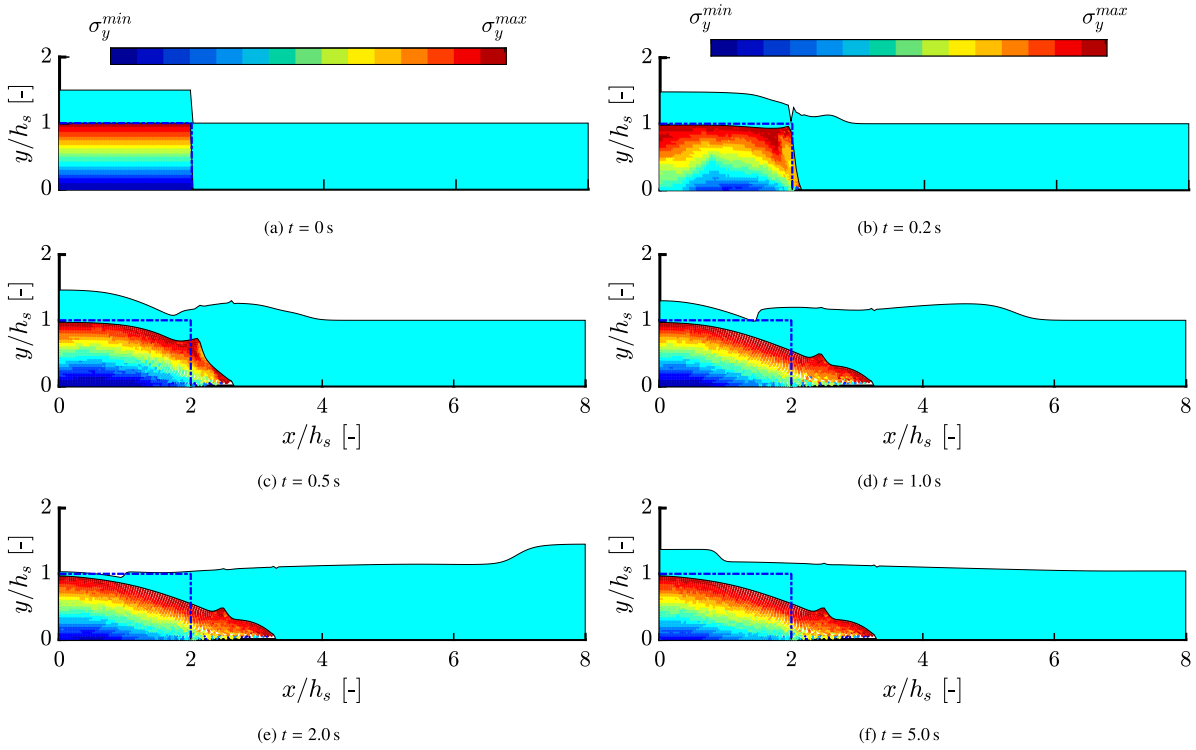

Fig. 13. Time evolution of the vertical stress contours and water free-surface profiles for clay column collapse in a dam-break flow with $R = 0.5$.

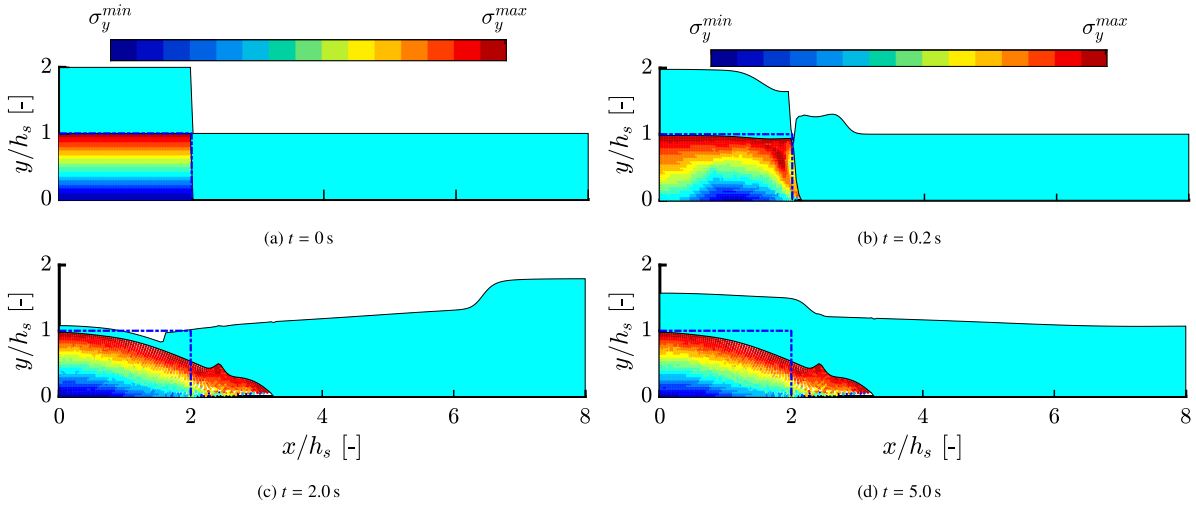

Fig. 14. Same as Fig. 13 but with $R = 1.0$.

Table 5
Computational results of the undrained clay column collapse in a dam-break flow with different values of R.

R	t = 0.5 s				t = 1.0 s				t = 5.0 s			
	$\Delta s/h_s$	η_{max}/h_s	$\lvert\bar{v}_s\rvert_{max}$	$\lvert\bar{u}_0\rvert_{max}$	$\Delta s/h_s$	η_{max}/h_s	$\lvert\bar{v}_s\rvert_{max}$	$\lvert\bar{u}_0\rvert_{max}$	$\Delta s/h_s$	η_{max}/h_s	$\lvert\bar{v}_s\rvert_{max}$	$\lvert\bar{u}_0\rvert_{max}$
0.5	0.633	1.461	0.651	0.405	1.240	1.297	0.432	0.616	1.230	1.371	0.089	0.032
1.0	0.589	1.943	0.618	1.064	1.186	1.458	0.413	0.762	1.229	1.572	0.085	0.215
2.0	0.560	2.581	0.569	1.816	1.015	1.710	0.386	1.316	1.032	1.606	0.080	0.398

[a] $\lvert\bar{u}_0\rvert_{max}$ – maximum value of dimensionless water velocity $\lvert\bar{u}_0\rvert/\sqrt{gh_s}$.
[b] $\lvert\bar{v}_s\rvert_{max}$ – maximum value of dimensionless soil velocity $\lvert\bar{v}_s\rvert/\sqrt{gh_s}$.

and consistent results during the large deformation analysis of soil and it has well captured the generation and propagation of shallow water waves. In particular, two fully coupled examples, involving clay column-induced shallow water waves and a dam-break simulation,

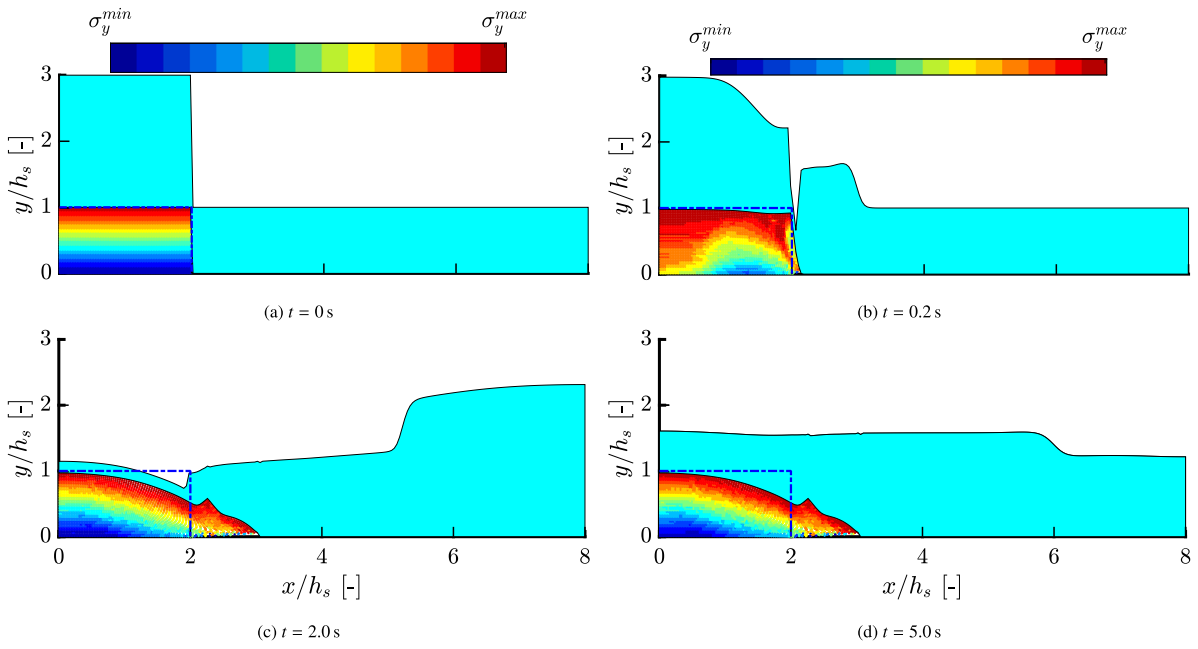

Fig. 15. Same as Fig. 13 but with $R = 2.0$.

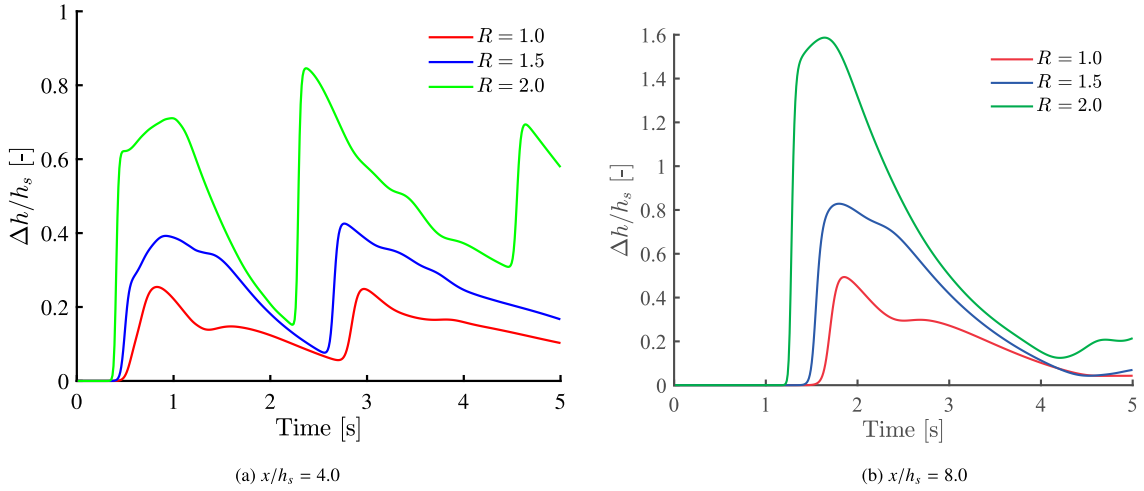

Fig. 16. Time evolution of water free-surface profiles for the problem of clay column collapse in a dam-break flow at two different gauges, (a) $x/h_s = 4$ and (b) $x/h_s = 8$.

have been used to demonstrate the good performance of the proposed hybrid material point/finite volume method for problems involving different inertial and deformation regimes. Future work will be devoted to validating the performance of the proposed hybrid method for large-deformation analyses through comparisons with experimental and field data. In addition, more challenging large-deformation problems with an advanced fully coupled MPM solver and allowing water inflow/outflow through the coupling surface will be beneficial for a better understanding of landslides that trigger natural hazards such as tsunamis.

CRediT authorship contribution statement

Xiangcou Zheng: Methodology, Software, Validation, Formal analysis, Visualization, Writing – original draft, Writing – review & editing. **Mohammed Seaid:** Conceptualization, Methodology, Supervision, Funding acquisition, Writing – review & editing. **Federico Pisanò:** Methodology, Supervision, Writing – review & editing. **Michael A. Hicks:** Methodology, Supervision, Writing – review & editing. **Philip J. Vardon:** Methodology, Supervision, Writing – review & editing. **Nejan Huvaj:** Methodology, Supervision, Writing – review & editing. **Ashraf S. Osman:** Conceptualization, Methodology, Supervision, Funding acquisition, Writing – review & editing.

Declaration of competing interest

The authors declare that they have no known competing financial interests or personal relationships that could have appeared to influence the work reported in this paper.

Data availability

Data will be made available on request

Acknowledgements

This work is funded by the British Council under Newton Fund Institutional Link programme (Grant reference 62309484).

References

Abe, K., Soga, K., Bandara, S., 2013. Material point method for coupled hydromechanical problems. J. Geotech. Geoenviron. 140 (3), 04013033.

Aiabadi, S., Akhbar, M., Patel, R., 2010. Hybrid finite element/volume method for shallow water equtions. Internat. J. Numer. Methods Engrg. 83, 1719–1738.

Al-Ghosoun, A., 2021. Optimal Control for Studying Wave Energy in Hydraulic Systems (Ph.D. thesis). Durham University.

Al-Ghosoun, A., Osman, A.S., Seaid, M., 2021. A computational model for simulation of shallow water waves by elastic deformations in the topography. Commun. Comput. Phys. 29 (4), 1095–1124.

Andersen, S., 2009. Material-Point Analysis of Large-Strain Problems: Modelling of Landslides (Ph.D. thesis). Aalborg University.

Andersen, S., Andersen, L., 2010. Modelling of landslides with the material-point method. Comput. Geosci. 14 (1), 137–147.

Arvanitis, C., Delis, A., 2006. Behavior of finite volume schemes for hyperbolic conservation laws on adaptive redistributed spatial grids. SIAM J. Sci. Comput. 28, 1927–1956.

Bandara, S., Soga, K., 2015. Coupling of soil deformation and pore fluid flow using material point method. Comput. Geotech. 63, 199–214.

Bardenhagen, S.G., Kober, E.M., 2004. The generalized interpolation material point method. Comput. Model. Eng. Sci. 5 (6), 477–496.

Baumgarten, A.S., Couchman, B.L., Kamrin, K., 2021. A coupled finite volume and material point method for two-phase simulation of liquid–sediment and gas–sediment flows. Comput. Methods Appl. Mech. Engrg. 384, 113940.

Belytschko, T., Organ, D., Krongauz, Y., 1995. A coupled finite element-element-free Galerkin method. Comput. Mech. 17 (3), 186–195.

Benkhaldoun, F., Sari, S., Seaid, M., 2012. A flux-limiter method for dam-break flows over erodible sediment beds. Appl. Math. Model. 36 (10), 4847–4861.

Beuth, L., 2012. Formulation and Application of a Quasi-Static Material Point Method (Ph.D. thesis). University of Stuttgart.

Bisht, V., Salgado, R., Prezzi, M., 2021. Simulating penetration problems in incompressible materials using the material point method. Comput. Geotech. 133, 103593.

Bui, H.H., Fukagawa, R., Sako, K., Ohno, S., 2008. Lagrangian meshfree particles method (SPH) for large deformation and failure flows of geomaterial using elastic–plastic soil constitutive model. Int. J. Numer. Anal. Methods Geomech. 32 (12), 1537–1570.

Bui, H.H., Kodikara, J.K., Bouazza, A., Haque, A., Ranjith, P.G., 2014. A novel computational approach for large deformation and post-failure analyses of segmental retaining wall systems. Int. J. Numer. Anal. Methods Geomech. 38 (13), 1321–1340.

Ceccato, F., Beuth, L., Vermeer, P.A., Simonini, P., 2016. Two-phase material point method applied to the study of cone penetration. Comput. Geotech. 80, 440–452.

Ceccato, F., Bisson, A., Cola, S., 2020. Large displacement numerical study of 3D plate anchors. Eur. J. Environ. Civ. Eng. 24 (4), 520–538.

Charlton, T.J., 2018. An Implicit Generalised Interpolation Material Point Method for Large Deformation and Gradient Elasto-Plasticity (Ph.D. thesis). Durham University.

Chen, C., Shen, C., Chen, C., Cheng, M., 2010. Stability analysis of an oceanic structure using the Lyapunov method. Eng. Comput. 27, 186–204.

Coetzee, C., Vermeer, P., Basson, A., 2005. The modelling of anchors using the material point method. Int. J. Numer. Anal. Methods Geomech. 29 (9), 879–895.

Coombs, W.M., Augarde, C.E., Brennan, A.J., Brown, M.J., Charlton, T.J., Knappett, J.A., Motlagh, Y.G., Wang, L., 2020. On Lagrangian mechanics and the implicit material point method for large deformation elasto-plasticity. Comput. Methods Appl. Mech. Engrg. 358, 112622.

Coombs, W.M., Charlton, T.J., Cortis, M., Augarde, C.E., 2018. Overcoming volumetric locking in material point methods. Comput. Methods Appl. Mech. Engrg. 333, 1–21.

Cremonesi, M., Frangi, A., Perego, U., 2011. A Lagrangian finite element approach for the simulation of water-waves induced by landslides. Comput. Struct. 89 (11–12), 1086–1093.

de Vaucorbeil, A., Nguyen, V.P., Hutchinson, C.R., 2020. A total-Lagrangian material point method for solid mechanics problems involving large deformations. Comput. Methods Appl. Mech. Engrg. 360, 112783.

Della Vecchia, G., Cremonesi, M., Pisanò, F., 2019. On the rheological characterisation of liquefied sands through the dam-breaking test. Int. J. Numer. Anal. Methods Geomech. 43 (7), 1410–1425.

Du, W., Sheng, Q., Fu, X., Chen, J., Zhou, Y., 2021. Extensions of the two-phase double-point material point method to simulate the landslide-induced surge process. Eng. Anal. Bound. Elem. 133, 362–375.

Feng, R., Fourtakas, G., Rogers, B.D., Lombardi, D., 2021. Large deformation analysis of granular materials with stabilized and noise-free stress treatment in smoothed particle hydrodynamics (SPH). Comput. Geotech. 138, 104356.

Fuhrman, D., Madsen, P., 2009. Tsunami generation, propagation, and run-up with a high order Boussinesq model. Coast. Eng. 56, 747–758.

Gingold, R.A., Monaghan, J.J., 1977. Smoothed particle hydrodynamics: theory and application to non-spherical stars. Mon. Not. R. Astron. Soc. 181 (3), 375–389.

González Acosta, L.J., Vardon, P.J., Remmerswaal, G., Hicks, M.A., 2020. An investigation of stress inaccuracies and proposed solution in the material point method. Comput. Mech. 65 (2), 555–581.

Hargarten, S., Robl, J., 2019. Modeling rapid mass movements using the shallow water equations. Nat. Hazards Earth Syst. Sci. 2, 6775–6809.

Iaconeta, I., Larese, A., Rossi, R., Oñate, E., 2019. A stabilized mixed implicit material point method for non-linear incompressible solid mechanics. Comput. Mech. 63 (6), 1243–1260.

Jassim, I., Stolle, D., Vermeer, P., 2013. Two-phase dynamic analysis by material point method. Int. J. Numer. Anal. Methods Geomech. 37 (15), 2502–2522.

Kiriyama, T., Higo, Y., 2020. Arbitrary particle domain interpolation method and application to problems of geomaterial deformation. Soils Found. 60 (6), 1422–1439.

Kirstetter, G., Hu, J., Delestre, O., Darboux, F., Lagree, P., Popinet, S., Fullana, J., Josserand, C., 2016. Modeling rain-driven overland flow empirical versus analytical friction terms in the shallow water approximation. J. Hydrol. 536, 1–9.

Koukouselis, A., Chatziioannou, K., Mistakidis, E., Katsardi, V., 2019. Development of an equivalent static method for the approximation of the dynamic response of offshore structures. Eng. Comput. 36, 1121–1141.

Kularathna, S., Liang, W., Zhao, T., Chandra, B., Zhao, J., Soga, K., 2021. A semi-implicit material point method based on fractional-step method for saturated soil. Int. J. Numer. Anal. Methods Geomech. 45 (10), 1405–1436.

Kularathna, S., Soga, K., 2017. Implicit formulation of material point method for analysis of incompressible materials. Comput. Methods Appl. Mech. Engrg. 313, 673–686.

Lei, X., He, S., Wu, L., 2021. Stabilized generalized interpolation material point method for coupled hydro-mechanical problems. Comput. Part. Mech. 8, 701–720.

Li, B., Habbal, F., Ortiz, M., 2010. Optimal transportation meshfree approximation schemes for fluid and plastic flows. Internat. J. Numer. Methods Engrg. 83 (12), 1541–1579.

Li, B., Stalzer, M., Ortiz, M., 2014. A massively parallel implementation of the optimal transportation meshfree method for explicit solid dynamics. Internat. J. Numer. Methods Engrg. 100 (1), 40–61.

Liang, W., Zhao, J., Wu, H., Soga, K., 2021. Multiscale modeling of anchor pullout in sand. J. Geotech. Geoenviron. 147 (9), 04021091.

Liu, C.Q., Sun, Q.C., Jin, F., Zhou, G.G., 2017. A fully coupled hydro-mechanical material point method for saturated dense granular materials. Powder Technol. 314, 110–120.

Luan, M., Qu, P., Jeng, D., guo, Y., Yang, Q., 2008. Dynamic response of a porous seabed-pipeline interaction under wave loading: Soil-pipeline contact effects and inertial effects. Comput. Geotech. 35, 173–186.

Magda, W., 1997. Wave-induced uplift force on a submarine pipeline buried in a compressible seabed. Ocean Eng. 24, 551–576.

Martinelli, M., Galavi, V., 2021. Investigation of the material point method in the simulation of cone penetration tests in dry sand. Comput. Geotech. 130, 103923.

Mast, C., Mackenzie-Helnwein, P., Arduino, P., Miller, G.R., Shin, W., 2012. Mitigating kinematic locking in the material point method. J. Comput. Phys. 231 (16), 5351–5373.

Matsuo, T., Mori, K., Hiraoka, N., Sun, M., Bui, H.H., Fukagawa, R., 2016. Study of SPH simulation on tunnel face collapse. GEOMATE J. 10 (22), 2077–2082.

Monaghan, J.J., 1994. Simulating free surface flows with SPH. J. Comput. Phys. 110 (2), 399–406.

Monforte, L., Carbonell, J.M., Arroyo, M., Gens, A., 2017. Performance of mixed formulations for the particle finite element method in soil mechanics problems. Comput. Part. Mech. 4 (3), 269–284.

Navas, P., Rena, C.Y., López-Querol, S., Li, B., 2016. Dynamic consolidation problems in saturated soils solved through u–w formulation in a LME meshfree framework. Comput. Geotech. 79, 55–72.

Navas, P., Sanavia, L., López-Querol, S., Rena, C.Y., 2018. Explicit meshfree solution for large deformation dynamic problems in saturated porous media. Acta Geotech. 13 (2), 227–242.

Nazem, M., Sheng, D., Carter, J.P., Sloan, S.W., 2008. Arbitrary Lagrangian–Eulerian method for large-strain consolidation problems. Int. J. Numer. Anal. Methods Geomech. 32, 1023–1050.

Nguyen, C.T., Nguyen, C.T., Bui, H.H., Nguyen, G.D., Fukagawa, R., 2017. A new SPH-based approach to simulation of granular flows using viscous damping and stress regularisation. Landslides 14 (1), 69–81.

Okusa, S., 1985. Measurements of wave-induced pore pressure in submarine sediments under various marine conditions. Mar. Geotechnol. 6, 119–144.

Okusa, S., Uchilda, A., 1980. Pore-water pressure change in submarine sediments due to waves. Mar. Geotechnol. 4, 145–160.

Oñate, E., Idelsohn, S.R., Del Pin, F., Aubry, R., 2004. The particle finite element method—an overview. Int. J. Comput. Methods 1 (02), 267–307.

Pastor, M., Blanc, T., Haddad, B., Petrone, S., Morles, M.S., Drempetic, V., Issler, D., Crosta, G., Cascini, L., Sorbino, G., et al., 2014. Application of a SPH depth-integrated model to landslide run-out analysis. Landslides 11 (5), 793–812.

Pastor, M., Yague, A., Stickle, M., Manzanal, D., Mira, P., 2018. A two-phase SPH model for debris flow propagation. Int. J. Numer. Anal. Methods Geomech. 42 (3), 418–448.

Pudjaprasetya, S., Ribal, A., 2009. Numerical solution of Saint Venant equation to study floods in rivers. Coast. Eng. 56, 747–758.

Pudykiewicz, J., Staniforth, A., 1984. Some properties and comparative performance of the semi-Lagrangian method of robert in the solution of advection-diffusion equation. Atoms. Ocean 22, 283–308.

Ramadan, K., Hassan, H., Hanna, S., 2011. Modeling of tsunami generation and propagation by a spreading curvilinear seismic faulting in linearized shallow-water wave theory. Appl. Math. Model. 35, 61–79.
Roe, P., 1981. Approximate Riemann solvers, parameter vectors, and different schemes. J. Comput. Phys. 43, 357–372.
Sadeghirad, A., Brannon, R.M., Burghardt, J., 2011. A convected particle domain interpolation technique to extend applicability of the material point method for problems involving massive deformations. Internat. J. Numer. Methods Engrg. 86 (12), 1435–1456.
Soga, K., Alonso, E., Yerro, A., Kumar, K., Bandara, S., 2015. Trends in large-deformation analysis of landslide mass movements with particular emphasis on the material point method. Géotechnique 66 (3), 248–273.
Strang, G., 1968. On the construction and the comparison of difference schemes. J. Numer. Anal. 5, 506–517.
Sulsky, D., Chen, Z., Schreyer, H.L., 1994. A particle method for history-dependent materials. Comput. Methods Appl. Mech. Engrg. 118 (1–2), 179–196.
Sulsky, D., Zhou, S.J., Schreyer, H.L., 1995. Application of a particle-in-cell method to solid mechanics. Comput. Phys. Comm. 87 (1–2), 236–252.
Tran, Q.-A., Sołowski, W., 2019. Temporal and null-space filter for the material point method. Internat. J. Numer. Methods Engrg. 120 (3), 328–360.
Tsui, Y., Helfrich, C., 1983. Wave-induced pore pressure in submerged sand layer. J. Geotech. Eng. 109, 603–618.
Wang, D., Bienen, B., Nazem, M., Tian, Y., Zheng, J., Pucker, T., Randolph, M.F., 2015. Large deformation finite element analyses in geotechnical engineering. Comput. Geotech. 65, 104–114.
Wang, L., Coombs, W.M., Augarde, C.E., Cortis, M., Brown, M.J., Brennan, A.J., Knappett, J.A., Davidson, C., Richards, D., White, D.J., et al., 2021. An efficient and locking-free material point method for three-dimensional analysis with simplex elements. Internat. J. Numer. Methods Engrg. 122 (15), 3876–3899.
Wang, B., Vardon, P.J., Hicks, M.A., 2018. Rainfall-induced slope collapse with coupled material point method. Eng. Geol. 239, 1–12.
Wang, G., Zhang, Y., Nogami, T., 2004. Wave-induced seabed response analysis by radial point interpolation meshless method. Ocean Eng. 31, 21–42.
Wyser, E., Alkhimenkov, Y., Jaboyedoff, M., Podladchikov, Y.Y., 2020. A fast and efficient MATLAB-based MPM solver: fMPMM-solver v1.1. Geosci. Model. Dev. 13 (12), 6265–6284.
Yerro, A., Soga, K., Bray, J., 2019. Runout evaluation of oso landslide with the material point method. Can. Geotech. J. 56 (9), 1304–1317.
Yuan, W.H., Liu, K., Zhang, W., Dai, B., Wang, Y., 2020. Dynamic modeling of large deformation slope failure using smoothed particle finite element method. Landslides 1–13.
Yuan, W.H., Wang, H.C., Liu, K., Zhang, W., Wang, D., Wang, Y., 2021a. Analysis of large deformation geotechnical problems using implicit generalized interpolation material point method. J. Zhejiang Univ. Sci. A 22 (11), 909–923.
Yuan, W.H., Wang, H.-C., Zhang, W., Dai, B.-B., Liu, K., Wang, Y., 2021b. Particle finite element method implementation for large deformation analysis using abaqus. Acta Geotech. 1–14.
Zabala, F., Alonso, E., 2011. Progressive failure of aznalcóllar dam using the material point method. Géotechnique 61 (9), 795–808.
Zen, K., Yamazaki, H., 1991. Field observation and analysis of wave-induced liquefaction in seabed. Soils Found. 31, 161–179.
Zhang, H.W., Wang, K.P., Chen, Z., 2009. Material point method for dynamic analysis of saturated porous media under external contact/impact of solid bodies. Comput. Methods Appl. Mech. Engrg. 198 (17–20), 1456–1472.
Zhang, H.W., Wang, K.P., Zhang, Z., 2007. Material point method for numerical simulation of failure phenomena in multiphase porous media. In: Computational Mechanics: International Symposium on Computational Mechanics. Springer, pp. 36–47.
Zhang, X., Xu, C., Han, Y., 2015. Three-dimensional poro-elasto-plastic model for wave-induced seabed response around submarine pipeline. Soil Dyn. Earthq. Eng. 69, 163–171.
Zhang, H., Zhang, M., Ji, Y., Wang, Y., Xu, T., 2019. Numerical study of tsunami wave run-up and land inundation on coastal vegetated beaches. Comput. Geosci. 132, 9–22.
Zhang, F., Zhang, X., Sze, K.Y., Lian, Y., Liu, Y., 2017. Incompressible material point method for free surface flow. J. Comput. Phys. 330, 92–110.
Zhao, Y., Choo, J., 2020. Stabilized material point methods for coupled large deformation and fluid flow in porous materials. Comput. Methods Appl. Mech. Engrg. 362, 112742.
Zhao, K.L., Qiu, L.C., Liu, Y., 2022. Two-layer two-phase material point method simulation of granular landslides and generated tsunami waves. Phys. Fluids 34 (12), 123312.
Zheng, X.C., 2022. Stabilised Material Point Method for Fluid-Saturated Geomaterials (Ph.D. thesis). Delft University of Technology.
Zheng, Y.G., Gao, F., Zhang, H.W., Lu, M.K., 2013. Improved convected particle domain interpolation method for coupled dynamic analysis of fully saturated porous media involving large deformation. Comput. Methods Appl. Mech. Engrg. 257, 150–163.
Zheng, X.C., Pisanò, F., Vardon, P.J., Hicks, M.A., 2021. An explicit stabilised material point method for coupled hydromechanical problems in two-phase porous media. Comput. Geotech. 135, 104112.
Zheng, X.C., Pisanò, F., Vardon, P.J., Hicks, M.A., 2022. Fully implicit, stabilised MPM simulation of large-deformation problems in two-phase elastoplastic geomaterials. Comput. Geotech. 147, 104771.